Geotechnical rheological modeling of ballasted railway tracks considering the effect of principal stress rotation

Piyush Punetha[1] and Sanjay Nimbalkar[2]✉

[1]Ph.D. Candidate, School of Civil and Environmental Engineering, Faculty of Engineering and Information Technology, University of Technology Sydney, NSW 2007, Australia. Email: Piyush.Punetha@student.uts.edu.au, ORCID: 0000-0002-0812-4708.

[2]Senior Lecturer, School of Civil and Environmental Engineering, Faculty of Engineering and Information Technology, University of Technology Sydney, NSW 2007, Australia. Email: Sanjay.Nimbalkar@uts.edu.au, ORCID: 0000-0002-1538-3396.

✉Corresponding Author: Sanjay Nimbalkar (School of Civil and Environmental Engineering, Faculty of Engineering and Information Technology, University of Technology Sydney, NSW 2007, Australia. Phone no.: +61 2 95141819. Email: Sanjay.Nimbalkar@uts.edu.au)

ABSTRACT

The rotation of principal stress direction experienced by the soil elements in a railway track substructure during a train passage influences the magnitude of accumulated settlement. However, the existing methods to evaluate the track response under repeated train loads disregard the influence of principal stress rotation (PSR). This article presents a novel approach for assessing the behavior of ballasted railway tracks incorporating the contribution of PSR on track deformation. The proposed technique employs a geotechnical rheological model to evaluate the track behavior, in which the material plasticity is captured through plastic slider elements. The influence of PSR is accounted for by extending an existing constitutive relationship for the slider elements for the substructure layers, which is successfully validated against experimental data reported in the literature. The results reveal that PSR causes significant cumulative deformation in the substructure layers, and disregarding it in the analysis leads to inaccurate predictions. The proposed approach is then applied to an open track-bridge transition with heterogeneous support conditions, in which the differential settlement is found to be largely influenced by PSR. The findings from this study highlight the importance of including the effect of PSR in predictive models for a reliable evaluation of track performance.

Keywords: principal stress rotation; geotechnical rheological model; railway tracks; irrecoverable deformation; critical zones; differential settlement.

1. Introduction

A soil element in the track substructure experiences a complex change in the vertical, horizontal, and shear stresses during a train passage, which results in a rotation of the principal stress direction (McDonald and Raymond 1984; Powrie et al. 2007). Previous investigations have revealed that the principal stress rotation (PSR) significantly influences the accumulation of irrecoverable deformations in the tracks layers (Momoya et al. 2005; Wijewickreme and Vaid 2008; Gräbe and Clayton 2009; Ishikawa et al. 2011; Guo et al. 2018; Bian et al. 2020; Mamou et al. 2021). The additional deformation caused due to PSR contributes to the loss of stability and geometry of railway tracks. Therefore, the effects of PSR must be carefully addressed while evaluating the track response under moving wheel loads.

A comprehensive understanding of the track response under a large number of repeated train passages is crucial for its design and maintenance planning. The computational models are the most appropriate and economically viable tools to understand the behavior of railway tracks under various soil types, loads, and boundary conditions (Punetha et al. 2020; Varandas et al. 2020). A multitude of numerical and analytical methods with varying levels of complexity have been developed in the past to predict the behavior of railway tracks under repeated train passages (e.g., Mauer 1995; Suiker and de Borst 2003; Indraratna and Nimbalkar 2013; Li et al. 2018; Shih et al. 2019; Varandas et al. 2020; Grossoni et al. 2021). However, the predictive models that can incorporate the effect of PSR on track response are still scarce. Notwithstanding their practical value, the existing computational methodologies disregard the influence of PSR, which may limit the accuracy of the predicted response.

The accurate prediction of the track response is paramount for the critical zones in railway tracks that are highly susceptible to rapid degradation in track geometry (Li and Davis 2005). These zones include transitions between ballasted and slab tracks, between normal (or open) track and bridges, tunnels, viaducts or underpasses, and level crossings. The railway tracks in these sections show an inconsistent response along the length due to heterogeneous support conditions, resulting in uneven deformation or differential settlement. Consequently, these regions require frequent maintenance to ensure the safe and reliable operation of trains (Coelho et al. 2011; Sañudo et al. 2016; Wang et al. 2018).

To improve the performance of the critical zones, prior information of the magnitude of differential settlement accumulated in the substructure layers is indispensable. Consequently, several researchers resorted to numerical and analytical modeling techniques to investigate the behavior of these crucial regions and quantify the extent of the potential problem (e.g., Hunt 1997; Varandas et al. 2013; Paixão et al. 2015; Nielsen and Li 2018; Wang and Markine 2018; Shan et al. 2020; Punetha et al. 2021b). However, most of the existing methods neglect the additional deformation that is caused due to the PSR. Considerable efforts are still required to account for this critical aspect of soil behavior in the predictive models.

This study is aimed to provide a computational approach that incorporates the influence of PSR due to train-induced repeated loads on the response of the ballasted railway tracks. To this end, a novel geotechnical rheological model is employed in which the behavior of track layers is simulated using springs, dashpots, and slider elements. The effect of PSR is accounted for by modifying the constitutive relationships used for the plastic slider elements, which are validated against the experimental data available in the literature. The importance of including PSR in predicting track response is elucidated by comparing the results with and without PSR inclusion. Subsequently, the computational approach is applied to an open track-bridge transition by incorporating the inhomogeneous support conditions associated with the critical zone, and the influence of PSR on its behavior is investigated. The practical utility of the present approach is demonstrated by examining the suitability of different countermeasures in improving the performance of the critical zone. The incorporation of the contribution of PSR in the computational approach to evaluate the behavior of ballasted railway tracks, especially at a critical zone, is the key novelty in this paper. The present study provides a valuable tool with enhanced capability of including the PSR effects for the practicing railway engineers to accurately predict the track response, especially in the critical zones.

2. Geotechnical rheological track model

The substructure of the ballasted rail tracks constitutes several geotechnical layers that undergo recoverable and irrecoverable deformations under the train-induced repeated loading (Selig and Waters 1994; Nimbalkar et al. 2020). In this study, a rheological model is employed to predict the response of a track substructure, comprising of three layers: ballast, subballast, and subgrade, under repeated train loads (Punetha et al. 2021a). Fig. 1 illustrates the geotechnical rheological model of a ballasted railway track. The substructure layers in the model are represented as a series of discrete elastic springs, viscous dampers, lumped masses, and plastic slider elements. The springs and dampers simulate the viscoelastic response while the slider elements capture the irrecoverable deformation in the track layers. The equations of motion for the track substructure layers can be obtained by applying the dynamic equilibrium condition in Fig. 1:

$$
\begin{aligned}
&\begin{bmatrix} m_{\mathrm{g}} & 0 & 0 \\ 0 & m_{\mathrm{s}} & 0 \\ 0 & 0 & m_{\mathrm{b}} \end{bmatrix}
\begin{Bmatrix} d\ddot{w}_{\mathrm{g,n}}(t) \\ d\ddot{w}_{\mathrm{s,n}}(t) \\ d\ddot{w}_{\mathrm{b,n}}(t) \end{Bmatrix}
+ \begin{bmatrix} c_{\mathrm{g}} + c_{\mathrm{s}} + 2c_{\mathrm{g}}^{s} & -c_{\mathrm{s}} & 0 \\ -c_{\mathrm{s}} & c_{\mathrm{s}} + c_{\mathrm{b}} + 2c_{\mathrm{s}}^{s} & -c_{\mathrm{b}} \\ 0 & -c_{\mathrm{b}} & c_{\mathrm{b}} + 2c_{\mathrm{b}}^{s} \end{bmatrix}
\begin{Bmatrix} d\dot{w}_{\mathrm{g,n}}(t) \\ d\dot{w}_{\mathrm{s,n}}(t) \\ d\dot{w}_{\mathrm{b,n}}(t) \end{Bmatrix} \\
&+ \begin{bmatrix} k_{\mathrm{g}} + k_{\mathrm{s}} + 2k_{\mathrm{g}}^{s} & -k_{\mathrm{s}} & 0 \\ -k_{\mathrm{s}} & k_{\mathrm{s}} + k_{\mathrm{b}} + 2k_{\mathrm{s}}^{s} & -k_{\mathrm{b}} \\ 0 & -k_{\mathrm{b}} & k_{\mathrm{b}} + 2k_{\mathrm{b}}^{s} \end{bmatrix}
\begin{Bmatrix} dw_{\mathrm{g,n}}(t) \\ dw_{\mathrm{s,n}}(t) \\ dw_{\mathrm{b,n}}(t) \end{Bmatrix}
- \begin{bmatrix} c_{\mathrm{g}} + 2c_{\mathrm{g}}^{s} & -c_{\mathrm{s}} & 0 \\ 2c_{\mathrm{s}}^{s} & c_{\mathrm{s}} + 2c_{\mathrm{s}}^{s} & -c_{\mathrm{b}} \\ 2c_{\mathrm{b}}^{s} & 2c_{\mathrm{b}}^{s} & c_{\mathrm{b}} + 2c_{\mathrm{b}}^{s} \end{bmatrix}
\begin{Bmatrix} d\dot{w}_{\mathrm{g,n}}^{p}(t) \\ d\dot{w}_{\mathrm{s,n}}^{p}(t) \\ d\dot{w}_{\mathrm{b,n}}^{p}(t) \end{Bmatrix} \\
&- \begin{bmatrix} k_{\mathrm{g}} + 2k_{\mathrm{g}}^{s} & -k_{\mathrm{s}} & 0 \\ 2k_{\mathrm{s}}^{s} & k_{\mathrm{s}} + 2k_{\mathrm{s}}^{s} & -k_{\mathrm{b}} \\ 2k_{\mathrm{b}}^{s} & 2k_{\mathrm{b}}^{s} & k_{\mathrm{b}} + 2k_{\mathrm{b}}^{s} \end{bmatrix}
\begin{Bmatrix} dw_{\mathrm{g,n}}^{p}(t) \\ dw_{\mathrm{s,n}}^{p}(t) \\ dw_{\mathrm{b,n}}^{p}(t) \end{Bmatrix}
- \begin{bmatrix} c_{\mathrm{g}}^{s} & 0 & 0 \\ 0 & c_{\mathrm{s}}^{s} & 0 \\ 0 & 0 & c_{\mathrm{b}}^{s} \end{bmatrix}
\begin{Bmatrix} d\dot{w}_{\mathrm{g,n}-1}(t) + d\dot{w}_{\mathrm{g,n}+1}(t) \\ d\dot{w}_{\mathrm{s,n}-1}(t) + d\dot{w}_{\mathrm{s,n}+1}(t) \\ d\dot{w}_{\mathrm{b,n}-1}(t) + d\dot{w}_{\mathrm{b,n}+1}(t) \end{Bmatrix}
- \begin{bmatrix} k_{\mathrm{g}}^{s} & 0 & 0 \\ 0 & k_{\mathrm{s}}^{s} & 0 \\ 0 & 0 & k_{\mathrm{b}}^{s} \end{bmatrix} \\
&\begin{Bmatrix} dw_{\mathrm{g,n}-1}(t) + dw_{\mathrm{g,n}+1}(t) \\ dw_{\mathrm{s,n}-1}(t) + dw_{\mathrm{s,n}+1}(t) \\ dw_{\mathrm{b,n}-1}(t) + dw_{\mathrm{b,n}+1}(t) \end{Bmatrix}
+ \begin{bmatrix} c_{\mathrm{g}}^{s} & 0 & 0 \\ c_{\mathrm{s}}^{s} & c_{\mathrm{s}}^{s} & 0 \\ c_{\mathrm{b}}^{s} & c_{\mathrm{b}}^{s} & c_{\mathrm{b}}^{s} \end{bmatrix}
\begin{Bmatrix} d\dot{w}_{\mathrm{g,n}-1}^{p}(t) + d\dot{w}_{\mathrm{g,n}+1}^{p}(t) \\ d\dot{w}_{\mathrm{s,n}-1}^{p}(t) + d\dot{w}_{\mathrm{s,n}+1}^{p}(t) \\ d\dot{w}_{\mathrm{b,n}-1}^{p}(t) + d\dot{w}_{\mathrm{b,n}+1}^{p}(t) \end{Bmatrix}
+ \begin{bmatrix} k_{\mathrm{g}}^{s} & 0 & 0 \\ k_{\mathrm{s}}^{s} & k_{\mathrm{s}}^{s} & 0 \\ k_{\mathrm{b}}^{s} & k_{\mathrm{b}}^{s} & k_{\mathrm{b}}^{s} \end{bmatrix} \\
&\begin{Bmatrix} dw_{\mathrm{g,n}-1}^{p}(t) + dw_{\mathrm{g,n}+1}^{p}(t) \\ dw_{\mathrm{s,n}-1}^{p}(t) + dw_{\mathrm{s,n}+1}^{p}(t) \\ dw_{\mathrm{b,n}-1}^{p}(t) + dw_{\mathrm{b,n}+1}^{p}(t) \end{Bmatrix}
= \begin{Bmatrix} 0 \\ 0 \\ dQ_{\mathrm{r,n}}(t) \end{Bmatrix}
\end{aligned}
\tag{1}
$$

where subscript *n* denotes the *n*th sleeper; subscripts *b*, *g*, and *s* represent the ballast, subgrade, and subballast layers, respectively; superscript *p* stands for the plastic component of the response; *d* represents the increment; w, $\dot{w}$, and $\ddot{w}$ denote the vertical displacement (m), velocity (m/s), and acceleration (m/s^2) of the substructure layers, respectively; c, k, and m represent the damping coefficient (Ns/m), normal stiffness (N/m), and vibrating mass (kg) of the substructure layers, respectively; c^s and k^s denote the shear damping coefficient (Ns/m) and shear stiffness (N/m), respectively; Q_r stands for the rail seat load (N).

Eq. (1) is solved at each time instant, t, for individual sleeper locations by using Newmark's numerical integration scheme to obtain the total response of the track substructure, which typically comprises a recoverable (viscoelastic) and an irrecoverable (plastic) component, expressed as:

$$\mathrm{d}W_{\boxdot}(t) = \mathrm{d}W^{ve}_{\boxdot}(t) + \mathrm{d}W^{p}_{\boxdot}(t) \tag{2}$$

where the symbol $\boxdot$ stands for any of the substructure layers and can be b, g, or s; superscripts p and ve denote the plastic and the viscoelastic component of the response, respectively; W is the vertical deformation. The magnitude of the irrecoverable component in eq. (2) depends on the state of the plastic slider element. If this element is inactive, the total response is essentially viscoelastic [$dW^{p}_{\boxdot}(t) = 0$], whereas viscoelastic-plastic behavior is simulated if this element is active [$dW^{p}_{\boxdot}(t) \neq 0$]. The activation or deactivation of this element is controlled by the loading-unloading or Kuhn-Tucker relations (Simo and Hughes 1998). Accordingly, the slider element is activated when its yield criterion is met and remains satisfied. During the active state, the movement incurred in the slider element is computed using appropriate constitutive relationships, which are discussed in the next section.

To solve eq. (1), the parameters such as rail seat load, mass, stiffness, and damping coefficient for the substructure layers are also required. The procedure to determine these parameters is comprehensively discussed elsewhere (see, for example, Punetha et al. 2021a) and typically requires the values of Young's modulus (E), Poisson's ratio (v), density (ρ), and thickness (h) of the track layers.

2.1 Constitutive relationships for plastic slider elements

2.1.1 *Ballast and subballast*

For granular layers such as ballast and subballast, the constitutive relationship is based on an extended version of the Nor-Sand model, which incorporates the effect of PSR by rendering the hardening of the yield surface as a function of the principal stress rotation angle (Jefferies et al. 2015). The formulation of this model is within the framework of critical state soil mechanics, and it employs an associated flow rule with isotropic hardening plasticity.

The plastic deformation behavior of the slider element for granular layers follows from eq. (3) (Jefferies and Shuttle 2011):

(3)
$$D^p = \frac{d\varepsilon_{\mathrm{v}}^p}{d\varepsilon_{\mathrm{q}}^p} = \overline{\overline{M}} - \frac{q}{p}$$

where superscript p represents the plastic component; double bar symbol ($\overline{\overline{\ }}$) stands for the image state or the condition of zero dilatancy ($D^{\mathrm{p}} = 0$) (Jefferies 1993); $d\varepsilon_{\mathrm{q}}$ and $d\varepsilon_{\mathrm{v}}$ are the deviatoric and volumetric strain increments, respectively; p and q are the mean effective and deviatoric stresses, respectively; $\overline{\overline{M}}$ is the critical stress ratio at image state expressed as (Jefferies and Been 2015):

(4)
$$\overline{\overline{M}} = \left(1 - \frac{N_{\mathrm{v}}\overline{\overline{\chi}}|\overline{\overline{\psi}}|}{M_{\mathrm{tc}}}\right)\left[M_{\mathrm{tc}} - \frac{M_{\mathrm{tc}}^2 \cos\left(\frac{3\theta}{2} + \frac{\pi}{4}\right)}{3 + M_{\mathrm{tc}}}\right]$$

where subscript *tc* stands for triaxial compression condition; N_{v} is a volumetric coupling parameter; $\overline{\overline{\psi}}$ is the image state parameter [$\overline{\overline{\psi}} = \psi + \lambda \ln\left(\overline{\overline{p}}/p\right)$]; ψ is the state parameter ($\psi = e - e_{\mathrm{c}}$); e_{c} is the critical void ratio ($e_{\mathrm{c}} = \Gamma - \lambda \ln p$); Γ is the critical void ratio at $p = 1$ kPa; λ is the slope of critical state line; χ relates maximum dilatancy with the state parameter, [$\overline{\overline{\chi}} = \chi_{\mathrm{tc}} / \left(1 - \lambda\chi_{\mathrm{tc}} / \overline{\overline{M}}_{\mathrm{tc}}\right)$]; Θ is Lode's angle.

The plastic deformation occurs in the slider element if the yield criterion, *f*, defined in eq. (5) is met and remains satisfied (Jefferies and Been 2015):

$$f = \frac{q}{p\bar{\bar{M}}} + \ln\left(\frac{p}{\bar{\bar{p}}}\right) - 1 = 0 \tag{5}$$

The hardening of the yield surface is governed by the following equation, which is a modified version of the formulation proposed by Jefferies et al. (2015):

$$\frac{d\bar{\bar{p}}}{\bar{\bar{p}}} = \frac{H\ \ \bar{\bar{M}}}{R_{\mathrm{gl}}\bar{\bar{M}}_{\mathrm{tc}}}\left(\frac{\bar{\bar{p}}}{p}\right)_{\alpha}^{-2}\left[e^{\left(\frac{-\bar{\bar{\chi}}\bar{\bar{\psi}}}{\bar{\bar{M}}_{\mathrm{tc}}}\right)} - \left(\frac{\bar{\bar{p}}}{p}\right)_{\alpha}\right]d\varepsilon_{\mathrm{q}}^{p} \tag{6}$$

where H is a hardening parameter. The modification from the original formulation is the introduction of parameter R_{gl} that controls the plastic strain accumulation under repeated loading conditions and is expressed as (Punetha et al. 2021a):

$$R_{\mathrm{gl}} = e^{-\frac{1}{a_{\mathrm{h}}}\left(1-\frac{\bar{\bar{p}}}{\bar{\bar{p}}_{\mathrm{c}}}\right)}\sqrt{\frac{\bar{\bar{p}} - \bar{\bar{p}}_{\mathrm{m}}}{\bar{\bar{p}}_{\mathrm{c}} - \bar{\bar{p}}_{\mathrm{m}}}} \tag{7}$$

where a_{h} is the cyclic hardening parameter; $\bar{\bar{p}}_{\mathrm{m}}$ is the minimum value of $\bar{\bar{p}}$ observed during repeated loading; $\bar{\bar{p}}_{\mathrm{c}}$ is a parameter that accumulates during the active state of the slider element under repeated loading conditions and is calculated as $\bar{\bar{p}}_{\mathrm{c}}(t + dt) = \bar{\bar{p}}_{\mathrm{c}}(t) + d\bar{\bar{p}}$ when the slider element is active and $\bar{\bar{p}}_{\mathrm{c}}(t + dt) = \bar{\bar{p}}_{\mathrm{c}}(t)$ when the slider element is inactive. It is assumed that the size of the yield surface shrinks isotropically during the unloading stage (see APPENDIX A). This method of reducing the size of yield surface during unloading was originally proposed by Carter et al. (1982).

The term $\left(\frac{\bar{\bar{p}}}{p}\right)_{\alpha}$ in eq. (6) accounts for the effect of PSR and is determined using the following equation (Jefferies et al. 2015):

$$\left(\frac{\bar{\bar{p}}}{p}\right)_{\alpha} = \left(\frac{\bar{\bar{p}}}{p} - \frac{1}{r}\right)\left[1 - Z\left(\frac{|d\alpha|}{180}\right)|\psi|\right] + \frac{1}{r} \tag{8}$$

where α is the angle between major principal stress direction and vertical (°); r is a constant known as the spacing ratio [taken as 2.71 (see Jefferies et al. 2015)]; Z is the plastic softening parameter. The parameter Z controls the size of the yield surface during the rotation of the principal stress direction.

The input parameters for the plastic slider elements for ballast and subballast include Γ, λ, M_{tc}, N_{v}, χ_{tc}, a_{h}, H and Z. The critical state parameters Γ and λ can be calibrated against the data derived from undrained and drained triaxial compression tests on loose to dense specimens (Jefferies and Shuttle 2002). The values of parameters M_{tc} and N_{v} can be obtained from the stress-dilatancy plots (peak stress ratio, $\eta_{\max}$, against maximum dilatancy, $D^{p}_{\max}$) derived from the triaxial compression test data. A trend-line is fitted through the plot whose intercept and slope gives the values of M_{tc} and (1-N_{v}), respectively. The value of parameter χ_{tc} is determined using the state-dilatancy plots ($D^{p}_{\max}$ against ψ at $D^{p}_{\max}$) derived from the triaxial compression test data. A trend-line passing along the origin is fitted through the plot whose slope gives χ_{tc}. The hardening parameter H is derived using an iterative forward modeling of drained triaxial tests (see Jefferies and Been 2015). The cyclic hardening parameter a_{h} is calibrating against the data obtained from multiple cyclic triaxial tests. The parameter Z can be calibrated against the data obtained from hollow cylinder torsional or cyclic simple shear tests using the iterative forward modeling approach, wherein initial values of Z are assumed and subsequently updated based on simulation results (see Jefferies et al. 2015).

2.1.2 Subgrade

The constitutive relationship adopted for the plastic slider element for subgrade is based on the elastoplastic model proposed by Ma et al. (2017), which has been extended in this study to consider the deformation induced by the PSR. The effect of PSR is accounted for by rendering the yield surface, potential surface, and hardening rule as a function of α. Sassa and

Sekiguchi (2001) have used a similar approach to incorporate the effect of PSR in the generalized plasticity model (see APPENDIX B).

The plastic deformation behavior of the slider element for the subgrade follows from eq. (9):

$$d\boldsymbol{\varepsilon}^{p}_{\mathrm{ij}} = \Lambda_{\mathrm{s}} \frac{\partial g}{\partial \hat{\boldsymbol{\sigma}}_{\mathrm{ij}}} \tag{9}$$

where hat symbol (^) represents the parameter in characteristic stress space (Lu et al. 2017); $d\boldsymbol{\varepsilon}^{p}_{\mathrm{ij}}$ is the plastic strain increment; Λ_{s} is a scalar (also known as the plastic multiplier); $\boldsymbol{\sigma}_{\mathrm{ij}}$ is the stress tensor; g is the potential function which has been modified to account for the effect of PSR:

$$g = \ln\left[1 + \frac{(2\xi - Z_{\alpha})}{Z_{\alpha}} \frac{\hat{\eta}^{2}}{\hat{M}_{\alpha}^{2}}\right] + \frac{(2\xi - Z_{\alpha})}{\xi} \ln\left(\frac{\hat{p}}{\hat{p}_{\mathrm{xg}}}\right) \tag{10}$$

where ξ is a constitutive parameter (Punetha et al. 2021a); η is the stress ratio ($\eta = q/p$); $\hat{p}_{\mathrm{xg}}$ is the intersection of the potential function with the $\hat{p}$ axis; $\hat{M}_{\alpha}$ and Z_{α} are expressed as:

$$\hat{M}_{\alpha} = \hat{M}(1 - s_{1\alpha} U_{\alpha}) \tag{11a}$$

$$Z_{\alpha} = 1 + s_{2\alpha} U_{\alpha} \tag{11b}$$

$$U_{\alpha} = \begin{cases} 1 - \cos(2\alpha), \text{ for } 0 \leq \alpha \leq 45^{\circ} \\ 1 - \cos(2|\alpha| - \pi), \text{ for } 45^{\circ} \leq |\alpha| \leq 90^{\circ} \end{cases} \tag{11c}$$

$$\hat{M} = 3 \frac{(1 + \sin\varphi_{\mathrm{c}})^{\xi} - (1 - \sin\varphi_{\mathrm{c}})^{\xi}}{2(1 - \sin\varphi_{\mathrm{c}})^{\xi} + (1 + \sin\varphi_{\mathrm{c}})^{\xi}} \tag{11d}$$

where M is the critical stress ratio; φ_{c} is the critical state friction angle under triaxial compression; $s_{1\alpha}$ and $s_{2\alpha}$ are the constitutive parameters to account for the effects of PSR. The parameters $s_{1\alpha}$ and $s_{2\alpha}$ control the reduction in M and variation in the slope of the stress-dilatancy plot, respectively, due to a rotation in principal stress direction, as revealed by the experimental findings (Symes et al. 1988) (see APPENDIX B).

The plastic multiplier Λ_{s} in eq. (9) is calculated as (Lu et al. 2019):

$$\Lambda_{\mathrm{s}} = \frac{-\left(\frac{\partial f}{\partial \hat{q}} d\hat{q} + \frac{\partial f}{\partial \hat{p}} d\hat{p}\right)}{\left(\frac{\partial g}{\partial \hat{p}}\right)\left(\frac{\partial f}{\partial \varepsilon_{\mathrm{v}}^{p}}\right)} \tag{12}$$

where $d\hat{p}$ and $d\hat{q}$ are the mean effective and deviatoric stress increments in the characteristic stress space, respectively; *f* is the modified yield criterion for the plastic slider element for subgrade, defined by:

$$f = \frac{(\lambda - \kappa)}{\xi(1 + e_0)}\left\{\frac{\overline{A}}{(2 - Z_{\alpha})}\ln\left[\frac{\left(\hat{\eta}^2 + \hat{M}_{\alpha}^2\right) + (1 - Z_{\alpha})\left(\hat{\eta}^2 - \hat{M}_{\alpha}^2\right)}{\left(\hat{\eta}_0^2 + \hat{M}_{\alpha}^2\right) + (1 - Z_{\alpha})\left(\hat{\eta}_0^2 - \hat{M}_{\alpha}^2\right)}\right] + \ln\left(\frac{\hat{p}}{\hat{p}_0}\right)\right\} - \int \frac{d\varepsilon_{\mathrm{v}}^{p}}{R} = 0 \tag{13}$$

where subscript *0* denotes initial condition; λ and κ are the slope of critical state and swelling lines, respectively; *e* is the void ratio; $\overline{A}$ is a parameter expressed as:

$$\overline{A} = A\frac{(2 - Z_{\alpha})\ln 2}{\ln\left(\frac{2}{Z_{\alpha}}\right)} \tag{14}$$

where *A* is a dimensionless constitutive parameter determined using the following equation (Lu et al. 2019):

$$A = \frac{\xi(\hat{N} - \hat{\Gamma})}{(\lambda - \kappa)\ln 2} \tag{15}$$

where $\hat{N}$ and $\hat{\Gamma}$ are the void ratio of normal compression line and critical state line at $\hat{p}$ =1 kPa, respectively. The yield surface defined in eq. (13) is smooth and convex in the characteristic stress space (see Fig. C1 in APPENDIX C).

The accumulation of irrecoverable deformation under repeated loading conditions is simulated using the concept of subloading surfaces with isotropic hardening (Hashiguchi 1989). Three subloading surfaces have been used, which are defined as follows:

$$f_{\mathrm{t}} = \frac{\overline{A}}{(2 - Z_{\alpha})}\ln\left[\frac{\left(\hat{\eta}^2 + \hat{M}_{\alpha}^2\right) + (1 - Z_{\alpha})(\hat{\eta}^2 - \hat{M}_{\alpha}^2)}{Z_{\alpha}\hat{M}_{\alpha}^2}\right] + \ln\left(\frac{\hat{p}}{\hat{p}_{\mathrm{xt}}}\right) = 0 \tag{16a}$$

$$f_{\mathrm{c}} = \frac{\bar{A}}{(2 - Z_{\alpha})} \ln \left[\frac{\left(\hat{\eta}^2 + \hat{M}_{\alpha}^2\right) + (1 - Z_{\alpha})(\hat{\eta}^2 - \hat{M}_{\alpha}^2)}{Z_{\alpha} \hat{M}_{\alpha}^2} \right] + \ln\left(\frac{\hat{p}}{\hat{p}_{\mathrm{xc}}}\right) = 0 \tag{16b}$$

$$f_{\mathrm{r}} = \frac{\bar{A}}{(2 - Z_{\alpha})} \ln \left[\frac{\left(\hat{\eta}^2 + \hat{M}_{\alpha}^2\right) + (1 - Z_{\alpha})(\hat{\eta}^2 - \hat{M}_{\alpha}^2)}{Z_{\alpha} \hat{M}_{\alpha}^2} \right] + \ln\left(\frac{\hat{p}}{\hat{p}_{\mathrm{xr}}}\right) = 0 \tag{16c}$$

where $\hat{p}_{\mathrm{xt}}$, $\hat{p}_{\mathrm{xc}}$ and $\hat{p}_{\mathrm{xr}}$ are the intersections of the transitional (f_{t}), current (f_{c}) and reference (f_{r}) surfaces with the $\hat{p}$ axis, respectively. The hardening parameter, *R*, is expressed as:

$$R = e^{-\frac{1}{a_{\mathrm{h}}(1 + 2U_{\alpha})}\left(1 - \frac{\hat{p}_{\mathrm{xc}}}{\hat{p}_{\mathrm{xr}}}\right)} \sqrt{\frac{\hat{p}_{\mathrm{xc}} - \hat{p}_{\mathrm{xt}}}{\hat{p}_{\mathrm{xr}} - \hat{p}_{\mathrm{xt}}}} \tag{17}$$

where a_{h} is the cyclic hardening parameter.

Substituting the value of g and Λ_{s} in eq. (9), the following relationship is obtained:

$$\begin{aligned} d\boldsymbol{\varepsilon}_{\mathrm{ij}}^{p} = \frac{R(\lambda - \kappa)}{\xi(1 + e_0)} \Bigg[& \frac{\left\{(1 - 2\bar{A})\hat{q}^2 + \hat{M}_{\alpha}^2\hat{p}^2 + (1 - Z_{\alpha})\left(\hat{q}^2 - \hat{M}_{\alpha}^2\hat{p}^2\right)\right\} d\hat{p}}{\hat{p}\left\{(\hat{q}^2 + \hat{M}_{\alpha}^2\hat{p}^2) + (1 - Z_{\alpha})(\hat{q}^2 - \hat{M}_{\alpha}^2\hat{p}^2)\right\}} \\ & + \frac{2\bar{A}\hat{q}\, d\hat{q}}{\left\{\left(\hat{q}^2 + \hat{M}_{\alpha}^2\hat{p}^2\right) + (1 - Z_{\alpha})\left(\hat{q}^2 - \hat{M}_{\alpha}^2\hat{p}^2\right)\right\}} \Bigg] \left[\frac{3\xi\hat{p}(\hat{\boldsymbol{\sigma}}_{\mathrm{ij}} - \hat{p}\delta_{\mathrm{ij}})}{Z_{\alpha}(\hat{M}_{\alpha}^2\hat{p}^2 - \hat{q}^2)} + \frac{\delta_{\mathrm{ij}}}{3} \right] \end{aligned} \tag{18}$$

where δ_{ij} is the Kronecker delta.

The aforementioned model can be used to describe the compressive behavior of the soil. To simulate the dilative behavior, the yield criterion is revised as:

$$f = \frac{(\lambda - \kappa)}{\xi(1 + e_0)} \left\{ \frac{\bar{A}}{(2 - Z_{\alpha})} \ln \left[\frac{\left(\hat{\eta}^2 + \hat{M}_{\alpha\mathrm{p}}^2\right) + (1 - Z_{\alpha})\left(\hat{\eta}^2 - \hat{M}_{\alpha\mathrm{p}}^2\right)}{\left(\hat{\eta}_0^2 + \hat{M}_{\alpha\mathrm{p}}^2\right) + (1 - Z_{\alpha})\left(\hat{\eta}_0^2 - \hat{M}_{\alpha\mathrm{p}}^2\right)} \right] + \ln\left(\frac{\hat{p}}{\hat{p}_0}\right) \right\} - \int \frac{d\varepsilon_{\mathrm{v}}^{p}}{R^*} = 0 \tag{19}$$

where $\hat{M}_{\alpha\mathrm{p}} = \hat{M}_{\mathrm{p}}(1 - s_{1\alpha}U_{\alpha})$; M_{p} is the peak stress ratio; R^* is a hardening parameter given by:

$$R^* = R\left(\frac{\hat{M}_{\alpha\mathrm{p}}}{\hat{M}_{\alpha}}\right)^2 \left(\frac{\hat{M}_{\alpha}^2\hat{p}^2 - \hat{q}^2}{\hat{M}_{\alpha\mathrm{p}}^2\hat{p}^2 - \hat{q}^2}\right) \tag{20}$$

The plastic strain increment can be obtained using eqs. (9), (12), and (19) as:

$$d\boldsymbol{\varepsilon}_{\mathrm{ij}}^{p} = \frac{R^{*}(\lambda-\kappa)}{\xi(1+e_0)}\left[\frac{\left\{(1-2\bar{A})\hat{q}^2+\hat{M}_{\alpha\mathrm{p}}^2\hat{p}^2+(1-Z_\alpha)\left(\hat{q}^2-\hat{M}_{\alpha\mathrm{p}}^2\hat{p}^2\right)\right\}d\hat{p}}{\hat{p}\left\{(\hat{q}^2+\hat{M}_{\alpha\mathrm{p}}^2\hat{p}^2)+(1-Z_\alpha)(\hat{q}^2-\hat{M}_{\alpha\mathrm{p}}^2\hat{p}^2)\right\}} + \frac{2\bar{A}\hat{q}\,d\hat{q}}{\left\{\left(\hat{q}^2+\hat{M}_{\alpha\mathrm{p}}^2\hat{p}^2\right)+(1-Z_\alpha)\left(\hat{q}^2-\hat{M}_{\alpha\mathrm{p}}^2\hat{p}^2\right)\right\}}\right]\left[\frac{3\xi\hat{p}(\hat{\boldsymbol{\sigma}}_{\mathrm{ij}}-\hat{p}\delta_{\mathrm{ij}})}{Z_\alpha(\hat{M}_{\alpha}^2\hat{p}^2-\hat{q}^2)}+\frac{\delta_{\mathrm{ij}}}{3}\right] \tag{21}$$

The input parameters for the plastic slider elements for subgrade include λ, κ, φ_{c}, M_{p}, ξ, A, a_{h}, $s_{1\alpha}$ and $s_{2\alpha}$. The critical state parameters λ and κ are determined using the data derived from isotropic compression and swelling tests. The parameter φ_{c} is the critical state friction angle obtained using the data from multiple triaxial compression tests. The parameter M_{p} is the stress ratio corresponding to the peak determined using the triaxial compression test data. The value of ξ is computed by solving the following equation:

$$\frac{(1+\sin\varphi_{\mathrm{c}})^{\xi}-(1-\sin\varphi_{\mathrm{c}})^{\xi}}{(1+\sin\varphi_{\mathrm{c}})^{\xi}+2(1-\sin\varphi_{\mathrm{c}})^{\xi}} = \frac{(1+\sin\varphi_{\mathrm{e}})^{\xi}-(1-\sin\varphi_{\mathrm{e}})^{\xi}}{(1-\sin\varphi_{\mathrm{e}})^{\xi}+2(1+\sin\varphi_{\mathrm{e}})^{\xi}} \tag{22}$$

where φ_{e} is the critical state friction angle derived using the data from triaxial extension tests. The value of parameter A is determined using eq. (15). The hardening parameter a_{h} is calibrated against the data obtained from multiple cyclic triaxial tests (or from cyclic hollow cylindrical torsional tests at $\alpha = 0°$). The PSR parameter $s_{1\alpha}$ can be obtained using the stress-dilatancy plots derived from the hollow cylindrical torsional test data (with constant α). A trend-line is fitted through the plot whose intercept gives the values of $\hat{M}_{\alpha}$ at different values of α. Subsequently, the values of $\hat{M}_{\alpha}$ are plotted against U_{α} [derived using eq. (11c)] and the parameter $s_{1\alpha}$ is derived using eq. (11a) and (11d). The value of PSR parameter $s_{2\alpha}$ is determined using the data derived from hollow cylindrical torsional tests conducted at various α values. First, a trend line is fitted through the $2\xi\hat{\eta}D^{p}$ versus $\hat{\eta}^2$ plot for different values of α. The slope of this line gives the value of $-Z_{\alpha}$. Next, the values of Z_{α} are plotted against U_{α} and the parameter $s_{2\alpha}$ is derived using eq. (11b).

It must be noted that the constitutive relationships for the plastic slider elements for granular layers and subgrade are based on continuum stress variables, such as p and q. These stress variables are determined using the modified Boussinesq solutions (Waterways Experiment Station 1954; Poulos and Davis 1974), in which multiple substructure layers are transformed to a single-layered material of equivalent thickness using the approach developed by Odemark (1949) and Hirai (2008). This technique of computing the continuum stress variables for the plastic slider elements complies with the existing methods (see Di Prisco and Vecchiotti 2006). In this study, all the stresses are considered effective stresses.

2.2 Model validation

The extended model for the slider element for subgrade is validated against the results of experimental investigations conducted by Cai et al. (2015), Wijewickreme and Vaid (2008), Yang (2013), and Wu et al. (2020). Table 1 lists the constitutive parameters used in the predictions.

Cai et al. (2015) studied the effect of principal stress rotation on the behavior of fine sand (relative density = 70%) using hollow cylinder torsional shear device under repeated loading conditions. Fig. 2(a) shows the cyclic stress waveforms used in the experimental investigation conducted by Cai et al. (2015). Fig. 2(b) shows the strain accumulation in the vertical direction with an increase in the number of load cycles at different cyclic vertical stress ratios (CVSR), which is the ratio of vertical stress amplitude ($\sigma_{\mathrm{z}}^{ampl}$) to two times of initial mean effective stress (p_0) [see Fig. 2(a)]. These results are for the tests without principal stress rotation as the value of cyclic shear stress ratio (CSSR) is 0, which is the ratio of shear stress amplitude ($\tau_{\mathrm{z}\theta}^{ampl}$) to $\sigma_{\mathrm{z}}^{ampl}$. It is observed from Fig. 2(b) that the predicted results are in close agreement with the experimental data. The model can satisfactorily reproduce the accumulation of vertical strain with an increase in the number of load cycles for different vertical stress amplitudes. Figs. 2(c) and 2(d) show the accumulation of vertical strain with an increase in the number of load cycles at CVSR of 0.15 and 0.25, respectively, for various CSSR values (i.e., for tests involving continuous principal stress rotation). It is apparent that the present model predicts the accumulation of vertical strain quite well in relation to the observed behavior in the laboratory investigations. Fig. 2(e) shows the accumulation of vertical strain with an increase in the number of load cycles at CVSR of 0.15 and at confining pressure (σ_c) of 125 kPa. It can be observed that the predicted results are in good agreement with the experimental data. The model can predict the strain accumulation with the number of load cycles at various confining pressures.

The model is also validated against the results of experimental investigations conducted by Wijewickreme and Vaid (2008) on loose Ottawa sand (relative density = 30%) using hollow cylinder torsional shear device under monotonic loading condition. Figs. 3(a) and 3(b) show the variation of stress ratio and volumetric strain with deviatoric strain, respectively, for three different cases: A3002R, M3451, and A0451. The major principal stress is oriented (and held constant) at 0° and 45° with the vertical direction for cases A3002R and A0451, respectively. For M3451, α is increased from 0 to 45° with an increase in stress ratio, R, from 1 to 2. It can be observed from Fig. 3 that the predicted results match reasonably well with the experimental data reported by Wijewickreme and Vaid (2008). The present model can predict the increase in strain generated due to the PSR for the cases when α is held constant and varied continuously.

Fig. 4 shows a comparison of the model predictions with the data reported by Yang (2013) for tests conducted on dense Leighton Buzzard sand (relative density = 75% – 77%) using small-strain hollow cylinder apparatus. It can be observed that the predicted results are in an acceptable agreement with the experimental data. The model can predict the dilative response (negative volumetric strain) of the dense sand and the reduction in stress ratio with an increase in α.

Fig. 5 compares the model predictions with the data reported by Wu et al. (2020) for tests conducted on Fontainebleau sand (relative density = 74%) using simple shear apparatus. It is observed that the model simulates the accumulation of volumetric strain with an increase in the number of load cycles reasonably well in comparison to the experimental data. It also simulates the increase in cumulative volumetric strain associated with an increase in the amplitude of cyclic shear stress. The predicted volumetric strain values after 5000 load cycles vary by 3% to 14% from the experimental results.

Thus, the present model can successfully predict the behavior of geomaterials under a rotation of principal stress directions. This model requires only two additional parameters ($s_{1\alpha}$ and $s_{2\alpha}$) than the existing model to describe the effect of PSR in a simple yet effective manner. The influence of parameters $s_{1\alpha}$ and $s_{2\alpha}$ on the response of geomaterials is discussed in APPENDIX D. It must be noted that other advanced constitutive models are also available to capture the effect of PSR on the behavior of geomaterials (for e.g., Lashkari and Latifi 2008; Yang and Yu 2013; Petalas et al. 2018). These models can also be used for the plastic slider elements for the track substructure layers.

3. Results and discussion

This section discusses the influence of PSR in the track response and elucidates the importance of considering this phenomenon for more accurate predictions. Table 2 shows the values of the input parameters used in the predictions. The ballast considered in the analysis is crushed basalt and is classified as poorly graded gravel (GP) as per ASTM D2487 (ASTM 2017). The mean particle size (D_{50}), largest grain size ($D_{\max}$), and uniformity coefficient (C_u) of the ballast are 24.2 mm, 38 mm, and 1.7, respectively (Suiker et al. 2005). The subballast is classified as well-graded sand with gravel (SW) as per ASTM D2487 (ASTM 2017). The values of D_{50}, $D_{\max}$, and C_u of subballast are 0.75 mm, 20 mm, and 6.3, respectively (Suiker et al. 2005). The subgrade soil is classified as poorly graded sand (SP) as per ASTM D 2487

(ASTM 2017). The values of D_{50}, $D_{\max}$, and C_u of subgrade soil are 0.17 mm, 2 mm, and 1.7, respectively. The parameters for the subgrade plastic slider are the same as that previously calibrated using the experimental data reported by Cai et al. (2015). The shear damping coefficient for the track layers is taken as 80 kNs/m (Zhai et al. 2004).

Note that the nominal value of axle load is considered as 25 t unless otherwise specified. Firstly, the predicted stresses and settlement are discussed to describe the effect of PSR on a standard track. Subsequently, the effect of PSR under various axle loads and granular layer thickness is investigated.

3.1 Stress variation due to moving load

Fig. 6 illustrates the stress variation experienced by the substructure layers below a sleeper due to a moving wheel load. The stresses have been normalized with respect to maximum sleeper-ballast contact pressure (σ_{sb}), similar to the approach by Yang et al. (2009). At time instant t_1, the wheel is to the left of the sleeper under consideration, generating positive shear stress in the soil elements below the desired sleeper. As the wheel approaches the sleeper under consideration, the shear stress decreases and becomes equal to 0 at time instant t_2. At instant t_2, the wheel is exactly above the considered sleeper; consequently, the soil elements experience only normal stresses. A reversal in shear stress direction occurs as soon as the wheel moves away from the sleeper under consideration (see Fig. 6). This variation of the shear stresses, as the wheel passes a sleeper location, leads to the rotation in the direction of the principal stresses.

Fig. 7(a) shows the variation of vertical, horizontal, and shear stresses with time for a soil element located 1200 mm below the sleeper bottom during a train passage. It is apparent that the shear stress direction reverses as the wheel passes a sleeper location, leading to PSR. Fig. 7(b) shows that the magnitude of principal stress rotation varies with depth below a sleeper. During a train passage, the peak value of α initially increases with depth from sleeper bottom up to a maximum value and then decreases with a further increase in depth. Thus, the rotation of principal stresses is much higher for the subballast layer and the top portion of the subgrade layer than the ballast layer. This observation becomes evident in Figs. 7(c) – 7(e), which show the variation of deviatoric stress with α during a train passage at a depth of 100 mm (within ballast), 350 mm (within subballast), and 1200 mm (within subgrade) from the sleeper bottom, respectively. The magnitude of α is minimal at a depth of 100 mm compared to that at 350 mm and 1200 mm from the sleeper bottom. Nonetheless, the deviatoric stress is the highest in the ballast layer and decreases with an increase in depth [see Figs. 7(c) – 7(e)].

3.2 Effect of principal stress rotation on track deformation

Fig. 8(a) shows the accumulation of settlement with tonnage, with and without the inclusion of the PSR. It can be observed that the settlement is much higher when PSR is considered as compared to the case in which it is neglected. After a tonnage of 1 million gross tonnes (MGT), the cumulative settlement is 4.1 mm higher if PSR is considered than when neglected [see Fig. 8(b)]. A similar behavior is observed after a tonnage of 5 MGT [see Fig. 8(c)]. Moreover, after a cumulative tonnage of 20 MGT, the total settlement increases by 19.3% if PSR is included in the analysis [see Fig. 8(d)]. Thus, it is essential to consider the effect of PSR for accurate prediction of the track response. These results also reveal that PSR accelerates the track geometry degradation. In the absence of PSR, 20 mm settlement is accumulated after a tonnage of 2.9 MGT; however, this tonnage reduces to 0.45 MGT with PSR inclusion. These findings reflect the need to consider this critical aspect of soil behavior while computing the track response.

3.3 Influence of axle load

The rising trend of railways towards heavier axle loads to cater to the ever-increasing demands may lead to excessive deformation in the track substructure layers (Nimbalkar and Indraratna 2016). Therefore, the influence of axle load, Q_a, on the track response is investigated using the present approach by varying Q_a from 20 – 25 t. Fig. 9 shows the accumulation of settlement in the track substructure with tonnage at different axle loads. It is apparent that the cumulative settlement rises continuously with increasing axle load. A higher axle load generates larger stresses in the substructure layers, leading to increased settlement. The settlement at a cumulative tonnage of 20 MGT increases by 28.8 % on increasing the axle load from 20 – 25 t. It is also apparent from Fig. 9 that the settlement is underestimated if the phenomenon of PSR is disregarded. For 25 t axle load, the settlement predicted without PSR at a cumulative tonnage of 20 MGT is 16% less than when PSR is considered.

3.4 Influence of granular layer thickness

Increasing the granular layer thickness is one of the most economical and practical techniques to reduce the substructure layer deformations and improve track performance (Li and Selig 1998). For the tracks in which heavier axle loads are expected in the future, increasing the granular layer thickness may be a viable alternative for improving the track performance. Therefore, the granular layer thickness is varied between 450 – 900 mm to investigate its influence on the track behavior. The thickness is varied through two approaches: i) changing ballast thickness (h_b) from 300 – 750 mm at fixed subballast thickness (h_s) of 150 mm [Fig. 10(a)], and ii) changing h_s from 150 – 600 mm at fixed h_b of 300 mm [Fig. 10(b)]. The axle load for this analysis is taken as 25 t, which caused significant deformation in the track layers, as seen in the previous section.

Fig. 10 illustrates the accumulation of settlement with tonnage at different granular layer thicknesses. It can be observed that the cumulative settlement decreases with an increase in granular layer thickness. This occurs due to a reduction in stress transferred to the subgrade (which is the primary contributor to total settlement in this study) since the distance between the subgrade and sleeper bottom increases with granular layer thickness. Secondly, a thicker granular layer has higher stress spreading ability, which causes subgrade stress reduction (Li and Selig 1998). On comparing Figs. 10(a) and 10(b), it is apparent that the settlement reduces by a significant amount when ballast thickness is increased compared to the case when subballast thickness is increased. For instance, at a cumulative tonnage of 20 MGT, the settlement decreases by 52% with an increase in ballast thickness. However, this reduction reduces to 39.7% with an increase in subballast thickness. This behavior can be attributed to the higher strength of the ballast material than the subballast material.

Figs. 10(a) and 10(b) also show that the response is underestimated if the phenomenon of PSR is disregarded. This underestimation can seriously affect the selection of adequate granular layer thickness for a railway track, which is illustrated in Fig. 11. Assuming that the allowable settlement of the track substructure is 25 mm after a cumulative tonnage of 20 MGT. If the contribution of PSR is ignored, a granular layer thickness of 450 mm will suffice (h_b = 300 mm and h_s = 150 mm) (see Fig. 11). However, when PSR is considered, the required thickness rises to 525 mm (h_b = 375 mm and h_s = 150 mm). Thus, the selected thickness of the granular layer may be inadequate if the influence of PSR is disregarded during the response prediction.

4. Application to critical zones

The previous sections demonstrated the importance of including the effect of PSR for an accurate prediction of track response. The present approach with enhanced capabilities of including the PSR effect may prove beneficial for evaluating the performance of critical zones in railway tracks, for which the prediction of accurate track response is paramount. Therefore, the computational approach discussed in previous sections is extended to investigate the behavior of railway tracks in the critical zones. This is done by including the heterogeneous support conditions in the geotechnical rheological model, which are continually encountered in the track transitions. Fig. 12 shows the resulting rheological track model for a typical open track-bridge transition zone in which the track is supported by concrete deck on one side (stiffer side) and soil layers on the other (softer side). The substructure comprises ballast, subballast, and subgrade layers on the softer side, while the ballast layer supported on the concrete deck constitutes the substructure of the stiffer side. The concrete bridge deck and abutment are simulated as fixed supports owing to their negligible deformation as compared to the geotechnical layers. Note that a region adjacent to the bridge abutment, termed as improved zone, can also be provided to simulate the transitions in which engineered backfills or other mitigation strategies are employed to enhance the performance of the critical zones.

On applying the dynamic equilibrium condition in this model, the following equations of motion can be obtained:

$$
\begin{aligned}
&\begin{bmatrix} m_{\mathrm{g}} & 0 & 0 \\ 0 & m_{\mathrm{s}} & 0 \\ 0 & 0 & m_{\mathrm{b}} \end{bmatrix}\begin{Bmatrix} d\ddot{w}_{\mathrm{g,i}}(t) \\ d\ddot{w}_{\mathrm{s,i}}(t) \\ d\ddot{w}_{\mathrm{b,i}}(t) \end{Bmatrix} + \begin{bmatrix} c_{\mathrm{g}} + c_{\mathrm{s}} + 2c_{\mathrm{g}}^{s} & -c_{\mathrm{s}} & 0 \\ -c_{\mathrm{s}} & c_{\mathrm{s}} + c_{\mathrm{b}} + 2c_{\mathrm{s}}^{s} & -c_{\mathrm{b}} \\ 0 & -c_{\mathrm{b}} & c_{\mathrm{b}} + 2c_{\mathrm{b}}^{s} \end{bmatrix}\begin{Bmatrix} d\dot{w}_{\mathrm{g,i}}(t) \\ d\dot{w}_{\mathrm{s,i}}(t) \\ d\dot{w}_{\mathrm{b,i}}(t) \end{Bmatrix} \\
&\quad + \begin{bmatrix} k_{\mathrm{g}} + k_{\mathrm{s}} + 2k_{\mathrm{g}}^{s} & -k_{\mathrm{s}} & 0 \\ -k_{\mathrm{s}} & k_{\mathrm{s}} + k_{\mathrm{b}} + 2k_{\mathrm{s}}^{s} & -k_{\mathrm{b}} \\ 0 & -k_{\mathrm{b}} & k_{\mathrm{b}} + 2k_{\mathrm{b}}^{s} \end{bmatrix}\begin{Bmatrix} dw_{\mathrm{g,i}}(t) \\ dw_{\mathrm{s,i}}(t) \\ dw_{\mathrm{b,i}}(t) \end{Bmatrix} - \begin{bmatrix} c_{\mathrm{g}} + 2c_{\mathrm{g}}^{s} & -c_{\mathrm{s}} & 0 \\ 2c_{\mathrm{s}}^{s} & c_{\mathrm{s}} + 2c_{\mathrm{s}}^{s} & -c_{\mathrm{b}} \\ 2c_{\mathrm{b}}^{s} & 2c_{\mathrm{b}}^{s} & c_{\mathrm{b}} + 2c_{\mathrm{b}}^{s} \end{bmatrix}\Bigg(\\
&\begin{matrix} d\dot{w}_{\mathrm{g,i}}^{p}(t) \\ d\dot{w}_{\mathrm{s,i}}^{p}(t) \\ d\dot{w}_{\mathrm{b,i}}^{p}(t) \end{matrix}\Bigg\} - \begin{bmatrix} k_{\mathrm{g}} + 2k_{\mathrm{g}}^{s} & -k_{\mathrm{s}} & 0 \\ 2k_{\mathrm{s}}^{s} & k_{\mathrm{s}} + 2k_{\mathrm{s}}^{s} & -k_{\mathrm{b}} \\ 2k_{\mathrm{b}}^{s} & 2k_{\mathrm{b}}^{s} & k_{\mathrm{b}} + 2k_{\mathrm{b}}^{s} \end{bmatrix}\begin{Bmatrix} dw_{\mathrm{g,i}}^{p}(t) \\ dw_{\mathrm{s,i}}^{p}(t) \\ dw_{\mathrm{b,i}}^{p}(t) \end{Bmatrix} - \begin{bmatrix} c_{\mathrm{g}}^{s} & 0 & 0 \\ 0 & c_{\mathrm{s}}^{s} & 0 \\ 0 & 0 & c_{\mathrm{b}}^{s} \end{bmatrix}\Bigg\{ \begin{matrix} d\dot{w}_{\mathrm{g,i-1}}(t) + d\dot{w}_{\mathrm{g,i+1}}(t) \\ d\dot{w}_{\mathrm{s,i-1}}(t) + d\dot{w}_{\mathrm{s,i+1}}(t) \\ d\dot{w}_{\mathrm{b,i-1}}(t) + d\dot{w}_{\mathrm{b,i+1}}(t) \end{matrix} \\
&\Bigg\} - \begin{bmatrix} k_{\mathrm{g}}^{s} & 0 & 0 \\ 0 & k_{\mathrm{s}}^{s} & 0 \\ 0 & 0 & k_{\mathrm{b}}^{s} \end{bmatrix}\begin{Bmatrix} dw_{\mathrm{g,i-1}}(t) + dw_{\mathrm{g,i+1}}(t) \\ dw_{\mathrm{s,i-1}}(t) + dw_{\mathrm{s,i+1}}(t) \\ dw_{\mathrm{b,i-1}}(t) + dw_{\mathrm{b,i+1}}(t) \end{Bmatrix} + \begin{bmatrix} c_{\mathrm{g}}^{s} & 0 & 0 \\ c_{\mathrm{s}}^{s} & c_{\mathrm{s}}^{s} & 0 \\ c_{\mathrm{b}}^{s} & c_{\mathrm{b}}^{s} & c_{\mathrm{b}}^{s} \end{bmatrix}\begin{Bmatrix} d\dot{w}_{\mathrm{g,i-1}}^{p}(t) + d\dot{w}_{\mathrm{g,i+1}}^{p}(t) \\ d\dot{w}_{\mathrm{s,i-1}}^{p}(t) + d\dot{w}_{\mathrm{s,i+1}}^{p}(t) \\ d\dot{w}_{\mathrm{b,i-1}}^{p}(t) + d\dot{w}_{\mathrm{b,i+1}}^{p}(t) \end{Bmatrix} \\
&\quad + \begin{bmatrix} k_{\mathrm{g}}^{s} & 0 & 0 \\ k_{\mathrm{s}}^{s} & k_{\mathrm{s}}^{s} & 0 \\ k_{\mathrm{b}}^{s} & k_{\mathrm{b}}^{s} & k_{\mathrm{b}}^{s} \end{bmatrix}\begin{Bmatrix} dw_{\mathrm{g,i-1}}^{p}(t) + dw_{\mathrm{g,i+1}}^{p}(t) \\ dw_{\mathrm{s,i-1}}^{p}(t) + dw_{\mathrm{s,i+1}}^{p}(t) \\ dw_{\mathrm{b,i-1}}^{p}(t) + dw_{\mathrm{b,i+1}}^{p}(t) \end{Bmatrix} = \begin{Bmatrix} 0 \\ 0 \\ dQ_{\mathrm{r,i}}(t) \end{Bmatrix}
\end{aligned}
\tag{23a}
$$

$$
\begin{aligned}
&m_{\mathrm{b}}^{r} d\ddot{w}_{\mathrm{b,j}}(\mathrm{t}) + c_{\mathrm{b}}^{r}\left[d\dot{w}_{\mathrm{b,j}}(t) - d\dot{w}_{\mathrm{b,j}}^{p}(t)\right] + k_{\mathrm{b}}^{r}\left[dw_{\mathrm{b,j}}(t) - dw_{\mathrm{b,j}}^{p}(t)\right] + c_{\mathrm{b}}^{s,r}\big\langle 2\left[d\dot{w}_{\mathrm{b,j}}(t) - d\dot{w}_{\mathrm{b,j}}^{p}(t)\right] \\
&\quad - \left[d\dot{w}_{\mathrm{b,j-1}}(t) - d\dot{w}_{\mathrm{b,j-1}}^{p}(t)\right] - \left[d\dot{w}_{\mathrm{b,j+1}}(t) - d\dot{w}_{\mathrm{b,j+1}}^{p}(t)\right]\big\rangle + k_{\mathrm{b}}^{s,r}\big\langle 2\left[dw_{\mathrm{b,j}}(t)\right. \\
&\quad \left. - dw_{\mathrm{b,j}}^{p}(t)\right] - \left[dw_{\mathrm{b,j-1}}(t) - dw_{\mathrm{b,j-1}}^{p}(t)\right] - \left[dw_{\mathrm{b,j+1}}(t) - dw_{\mathrm{b,j+1}}^{p}(t)\right]\big\rangle \\
&\quad = dQ_{\mathrm{r,j}}^{r}(t)
\end{aligned}
\tag{23b}
$$

where subscripts *i* and *j* denote the *i*th and *j*th sleeper in the softer and stiffer side of the critical zone, respectively; superscripts *p* and *r* stand for the plastic component of the response and the stiffer side, respectively. The response of the critical zone is evaluated by solving eqs. (23a) and (23b) at each time instant for all the sleeper locations considered. Note that the origin of the coordinate system is considered to be at the onset of the stiffer side.

4.1 Validation of methodology

The validity of the present methodology to accurately simulate the behavior of critical zones with heterogeneous track support conditions is investigated by comparing the predicted results with the field data reported by Paixão et al. (2014) for a bridge approach in Portugal. Table 3 shows the value of the input parameters used in the simulation. Fig. 13 shows the variation of vertical track displacement with time during a single pass of *Alfa Pendular* train at two different locations of the critical zone. The field data (Paixão et al. 2014) and results predicted using the present method are shown by dotted and solid lines, respectively. It is evident that the predicted results are in very good agreement with the field data at both sections 2 and 4 (located at 14.7 m and 0.9 m from the bridge, respectively). The track displacement decreases slightly as the train moves from section 2 [supported by unbound granular material (UGM)] towards section 4 [supported by cement bound material (CBM)]. Thus, the present approach accurately simulates the response variation along the track length as observed in the field investigations.

The methodology is also validated against the field data reported by Mishra et al. (2017) for an open track-bridge transition in the United States. The track substructure at the softer side of the transition comprised of ballast, subballast (layer 2), and multiple subgrade layers (that are approximated as an equivalent single layer in the analysis). Table 3 shows the value of input parameters used in the simulation. Fig. 14 compares the accumulation of settlement in the three substructure layers under multiple train passages, predicted using the present methodology with the data recorded in the field. It can be observed that the predicted results are in reasonable agreement with the field data.

This validated model is now employed to investigate the performance of a typical open track-bridge transition shown in Fig. 12. The values of the parameters used in the analysis for the softer side and stiffer side are listed in Tables 2 and 4, respectively. Note that the nominal value of axle load is 25 t unless otherwise specified. Firstly, the behavior of a critical zone without any mitigation measure is studied at different axle loads. This investigation is particularly important for the transitions in which heavier axle loads are anticipated in the future. Subsequently, the practical utility of the present approach is demonstrated by investigating the effectiveness of two mitigation strategies in improving the performance of the critical zone. The effect of ignoring the deformations due to PSR is also highlighted by comparing the results with and without the inclusion of PSR.

4.2 Performance at different axle loads

The axle load is varied from 20 – 27 t to study its influence on the response of the critical zone. Fig. 15 shows the effect of axle load on the settlement accumulated along the track length in the open track-bridge transition after a cumulative tonnage of 20 MGT for two cases: i) when PSR is considered and ii) when PSR is neglected. It can be observed that the differential settlement in the critical zone rises continuously with increasing axle load. When PSR is considered, the differential settlement between the softer and stiffer sides increases by 46.1% on increasing the axle load from 20 – 27 t. The excessive differential settlement at higher axle loads is presumably due to an increase in the stresses in the substructure layers with axle load. In general, the track geometry degradation at the critical zones aggravates with an increase in the axle load. Consequently, the remedial measures intended to reduce this differential settlement become essential for the transitions in which heavier axle loads are expected in the future. It is also apparent from Fig. 15 that PSR increases the differential settlement between the softer and stiffer side of the critical zones. The predicted differential settlement at 25 t axle load is 16.3% less if PSR is ignored. Thus, the differential settlement is significantly underestimated if the phenomenon of PSR is neglected.

4.3 Improving the performance of the critical zones

The performance of a critical zone can be improved by reducing the differential settlement between the softer and stiffer side of the transition. However, the correct choice of the mitigation strategy is particularly crucial for achieving the desired performance. The geotechnical rheological model can be employed to study the efficacy of different countermeasures in alleviating the problems associated with the critical zones and furnish the most appropriate strategy. This capability of the rheological model is demonstrated by investigating the adequacy of two different mitigation strategies: i) using thicker granular layers to limit the stresses transmitted to the subgrade on the softer side and ii) increasing the subgrade strength. These countermeasures are aimed to reduce the subgrade deformation in the softer side of the transition, which is the key contributor to the differential settlement in this study.

4.3.1 Using thicker granular layers

The granular layer thickness in the softer side of the transition is varied from 450 – 900 mm to investigate its influence on the response of the critical zone. The required thickness of the granular layer (h_{gl}) is achieved by either increasing the ballast thickness from 300 – 750 mm or by increasing the subballast thickness from 150 – 600 mm. The thickness of only one layer is varied for an analysis, while the other layer is assigned a nominal value (see Table 2). Note that the thickness of the ballast layer at both the softer and stiffer side is kept identical. In the field, a thicker subballast layer can be furnished by replacing the underlying substructure layer with subballast to maintain the track level. Fig. 16(a) shows the influence of ballast thickness on the response of the critical zone with and without the inclusion of PSR. It can be observed that the differential settlement between the softer and stiffer side decreases with an increase in the ballast layer thickness. The differential settlement decreases by 86% with an increase in ballast thickness from 300 – 750 mm. This reduction is due to the fact that a thicker ballast layer spreads the load to a wider area; consequently, the stresses transferred to the underlying layers decrease (Selig and Waters 1994). This stress reduction leads to a decrease in the accumulated settlement. Nonetheless, the differential settlement is significantly underestimated for each granular layer thickness if PSR is disregarded.

Fig. 16(b) shows the influence of subballast thickness on the response of the critical zone with and without the inclusion of PSR. It can be observed that the differential settlement between the softer and stiffer side decreases with an increase in the subballast layer thickness. The differential settlement reduces by 41.6% with an increase in subballast thickness from 150 – 600 mm. This observation is reasonable since a thicker subballast layer spreads the load to a wider subgrade area and reduces the stress transferred to the subgrade (Selig and Waters 1994). However, the reduction in the differential settlement is smaller than that observed when ballast thickness is varied. This is presumably because the ballast material is much stronger as compared to the subballast material. It is also evident that the differential settlement is much higher if PSR is included compared to the case when it is ignored.

4.3.2 Improving the subgrade strength

The increment in subgrade strength (through ground improvement or geosynthetic reinforcement) is simulated by increasing the friction angle of the subgrade in the improved zone from 36 – 40°. Fig. 17(a) shows the variation of settlement along the track length after a cumulative tonnage of 20 MGT. It can be seen that improving the strength of the subgrade adjacent to the bridge approach (in the improved zone) reduces the differential settlement between the softer and stiffer side. The differential settlement decreases by 23% with an increase in φ_c from 36 – 40°. Fig. 17(b) shows the accumulation of settlement with tonnage in the softer side, improved zone and stiffer side of the transition. It can be observed that the settlement decreases along the length of the transition with the maximum settlement at the softer side (10.5 m from the bridge). It can also be seen that the settlement increases with PSR for all three zones. However, the increment is much higher for the softer side as compared to the stiffer side since the effect of PSR is more prominent in the subballast and subgrade layers as compared to the ballast layer (see Section 3.1).

Thus, the results show that the techniques such as thicker granular layers and strengthened subgrade effectively decrease the differential settlement in the critical zone. Increasing the thickness of the ballast layer is more effective in reducing differential settlements than increasing the subballast layer thickness. Moreover, the results also reveal that strengthening the subgrade soil using ground improvement techniques or geosynthetic reinforcements may also be a viable alternative, but it is less effective than using thicker granular layers. Overall, for the open track-bridge transition considered in this study, a simple strategy of using a thick ballast layer turns out to be the most effective technique for reducing the differential settlements. Thus, the present approach can be used to compare the effectiveness of different mitigation strategies in improving the track performance and selecting the most suitable technique for a particular critical zone.

5. Practical relevance, potential applications, limitations, and future scope

The computational methodology proposed in this paper provides a convenient means to evaluate the long-term performance of a ballasted railway track under train-induced repeated loading. Using this approach, a practicing railway engineer can evaluate the settlements accumulated at a section of a railway line over a specified amount of tonnage. This information would help in identifying the problematic sections along a railway line and in planning the maintenance cycles. The method can also be applied to transition zones to predict the magnitude of differential settlement accumulated after multiple train passages. Prior information of the differential settlements is crucial to optimize the design of the transition zones and improve the capacity of the track to allow heavier freight and high-speed passenger trains in the future. Moreover, as shown in the previous section, the proposed computational approach can be used to assess the adequacy of different countermeasures in improving the performance of the critical zones and select the most effective technique.

The limitations of the proposed computational approach are as follows:

- The present method considers train-induced loading only in the vertical direction. However, the ballasted railway tracks are also subjected to loading in longitudinal and transverse directions (Esveld 2001).
- In the present approach, the modified Boussinesq solutions are used to evaluate the stress distribution, which are based on the linear elasticity theory. However, the present method considers the elastoplastic behavior of the track constituent materials. Therefore, the accuracy of the present approach can be improved by evaluating the stress distribution based on plasticity theory. Nevertheless, the authors compared the stress distribution below a railway track, calculated using 3D finite element analysis, when the material behavior of substructure layers is considered as elastic and elastoplastic (see APPENDIX E). It was observed that the stress distribution calculated by considering elastoplastic material behavior was similar to that determined by assuming elastic material behavior (difference of about 12%).
- The approach does not consider the effect of seasonal fluctuations in the water content in the form of wetting and drying cycles, frost heave, and unsaturated geomaterials on the response of the ballasted railway track.

Future investigations shall address these limitations to improve the accuracy of the present approach. Moreover, the experimental investigations to distinguish between the track settlements occurring with and without PSR constitute the future scope of this study.

6. Conclusions

A computational approach is presented in this paper, which employs a novel geotechnical rheological model to simulate the response of ballasted railway tracks under train-induced loads. The key highlights of this study include:

- A simplified yet effective geotechnical rheological model with enhanced capability of capturing the effect of PSR for an accurate prediction of the track response. This is also the essential methodological contribution of this paper.
- Application of the rheological model to the critical zones by incorporating heterogeneous support conditions along the track length and predicting the magnitude of differential settlements accumulated over a specified period or tonnage.
- Using the computational approach to compare the effectiveness of different mitigation strategies in improving the performance of critical zones which helps in selecting the most appropriate strategy.

The rheological model used in this study considers the plasticity of track materials through plastic slider elements. The effect of PSR is accounted for in the model by modifying the constitutive relationship for the slider elements, which is successfully validated against the experimental data reported in the literature. A parametric study is conducted to investigate the influence of axle loads and granular layer thickness on track response, and the effect of PSR is highlighted by comparing the results with and without PSR inclusion. The results reveal that the deformation is significantly underestimated if PSR is neglected in the analysis, which may have severe consequences on selecting adequate granular layer thickness. The settlement after a cumulative tonnage of 20 MGT at 25 t axle load is found to be under-predicted by 16% if PSR is disregarded.

The application of the rheological model to an open track-bridge transition showed that the PSR increases the differential settlement between the softer and stiffer side of the critical zone. Moreover, the track geometry deterioration in the critical zone aggravates with axle load (46.1% increment with a rise in axle load from 20 – 27 t), which suggests the use of mitigation measures for the tracks in which heavier axle loads are anticipated in the future. An increase in granular layer thickness reduced the differential settlement in the critical zone, with ballast thickness increment more effective (up to 86% reduction) than subballast thickness increment (up to 41.6% reduction). The capability of the present approach to examine the suitability of different countermeasures in improving the performance of the critical zone exhibits its practical utility. Finally, the findings from this study emphasize the inclusion of the PSR effect in the computational or predictive models for an accurate prediction of the behavior of railway tracks.

Acknowledgements

This research is supported by an Australian Government Research Training Program Scholarship. The authors wish to thank the anonymous reviewers for providing valuable comments.

References

Altaee, A., Evgin, E., and Fellenius, B. 1992. Finite element validation of a bounding surface plasticity model. Computers & Structures, **42**(5): 825-832. doi:10.1016/0045-7949(92)90193-4.

Altuhafi, F.N., Jardine, R.J., Georgiannou, V.N., and Moinet, W.W. 2018. Effects of particle breakage and stress reversal on the behaviour of sand around displacement piles. Géotechnique, **68**(6): 546-555. doi:10.1680/jgeot.17.P.117.

ASTM. 2017. Standard practice for classification of soils for engineering purposes (Unified soil classification system). D2487. ASTM International, West Conshohocken, PA.

Bian, X., Li, W., Qian, Y., and Tutumluer, E. 2020. Analysing the effect of principal stress rotation on railway track settlement by discrete element method. Géotechnique, **70**(9): 803-821. doi:10.1680/jgeot.18.P.368.

Cai, Y., Sun, Q., Guo, L., Juang, C.H., and Wang, J. 2015. Permanent deformation characteristics of saturated sand under cyclic loading. Canadian Geotechnical Journal, **52**(6): 795-807. doi:10.1139/cgj-2014-0341.

Carter, J.P., Booker, J.R., and Wroth, C.P. 1982. A critical state soil model for cyclic loading. *In* Soil mechanics - transient and cyclic loads. *Edited by* G.N. Pande and O.C. Zienkiewicz. John Wiley and Sons Ltd. pp. 219-252.

Coelho, B., Hölscher, P., Priest, J., Powrie, W., and Barends, F. 2011. An assessment of transition zone performance. Proceedings of the Institution of Mechanical Engineers, Part F: Journal of Rail and Rapid Transit, **225**(2): 129-139. doi:10.1177/09544097jrrt389.

Di Prisco, C., and Vecchiotti, M. 2006. A rheological model for the description of boulder impacts on granular strata. Géotechnique, **56**(7): 469-482. doi:10.1680/geot.2006.56.7.469.

Esveld, C. 2001. Modern railway track. MRT-Productions, Delft, The Netherlands.

Gräbe, P.J., and Clayton, C.R.I. 2009. Effects of principal stress rotation on permanent deformation in rail track foundations. Journal of Geotechnical and Geoenvironmental Engineering, **135**(4): 555-565. doi:10.1061/(ASCE)1090-0241(2009)135:4(555).

Grossoni, I., Powrie, W., Zervos, A., Bezin, Y., and Le Pen, L. 2021. Modelling railway ballasted track settlement in vehicle-track interaction analysis. Transportation Geotechnics, **26**: 100433. doi:10.1016/j.trgeo.2020.100433.

Guo, L., Cai, Y., Jardine, R.J., Yang, Z., and Wang, J. 2018. Undrained behaviour of intact soft clay under cyclic paths that match vehicle loading conditions. Canadian Geotechnical Journal, **55**(1): 90-106. doi:10.1139/cgj-2016-0636.

Hashiguchi, K. 1989. Subloading surface model in unconventional plasticity. International Journal of Solids and Structures, **25**(8): 917-945. doi:10.1016/0020-7683(89)90038-3.

Hirai, H. 2008. Settlements and stresses of multi-layered grounds and improved grounds by equivalent elastic method. International Journal for Numerical and Analytical Methods in Geomechanics, **32**(5): 523-557. doi:10.1002/nag.636.

Hunt, H.E. 1997. Settlement of railway track near bridge abutments. Proceedings of the Institution of Civil Engineers - Transport, **123**(1): 68-73. doi:10.1680/itran.1997.29182.

Indraratna, B., and Nimbalkar, S. 2013. Stress-strain degradation response of railway ballast stabilized with geosynthetics. Journal of Geotechnical and Geoenvironmental Engineering, **139**(5): 684-700. doi:10.1061/(asce)gt.1943-5606.0000758.

Ishikawa, T., Sekine, E., and Miura, S. 2011. Cyclic deformation of granular material subjected to moving-wheel loads. Canadian Geotechnical Journal, **48**(5): 691-703. doi:10.1139/t10-099.

Jefferies, M., and Shuttle, D. 2011. On the operating critical friction ratio in general stress states. Géotechnique, **61**(8): 709-713. doi:10.1680/geot.9.T.032.

Jefferies, M., Shuttle, D., and Been, K. 2015. Principal stress rotation as cause of cyclic mobility. Geotechnical Research, **2**(2): 66-96. doi:10.1680/gr.15.00002.

Jefferies, M.G. 1993. Nor-Sand: a simple critical state model for sand. Géotechnique, **43**(1): 91-103. doi:10.1680/geot.1993.43.1.91.

Jefferies, M.G., and Shuttle, D.A. 2002. Dilatancy in general Cambridge-type models. Géotechnique, **52**(9): 625-638. doi:10.1680/geot.2002.52.9.625.

Jefferies, M.G., and Been, K. 2015. Soil liquefaction: a critical state approach. CRC press, Boca Raton, FL.

Kong, Y., Zhou, A., Shen, F., and Yao, Y. 2019. Stress–dilatancy relationship for fiber-reinforced sand and its modeling. Acta Geotechnica, **14**(6): 1871-1881. doi:10.1007/s11440-019-00834-6.

Lashkari, A., and Latifi, M. 2008. A non-coaxial constitutive model for sand deformation under rotation of principal stress axes. International Journal for Numerical and Analytical Methods in Geomechanics, **32**(9): 1051-1086. doi:10.1002/nag.659.

Li, D., and Selig, E.T. 1998. Method for railroad track foundation design. I: Development. Journal of Geotechnical and Geoenvironmental Engineering, **124**(4): 316-322. doi:10.1061/(asce)1090-0241(1998)124:4(316)

Li, D., and Davis, D. 2005. Transition of railroad bridge approaches. Journal of Geotechnical and Geoenvironmental Engineering, **131**(11): 1392-1398. doi:10.1061/(ASCE)1090-0241(2005)131:11(1392).

Li, D., Hyslip, J., Sussmann, T., and Chrismer, S. 2016. Railway geotechnics. Taylor and Francis, Boca Raton, USA.

Li, L., Nimbalkar, S., and Zhong, R. 2018. Finite element model of ballasted railway with infinite boundaries considering effects of moving train loads and Rayleigh waves. Soil Dynamics and Earthquake Engineering, **114**: 147-153. doi:10.1016/j.soildyn.2018.06.033.

Lu, D., Li, X., Du, X., and Liang, J. 2019. A simple 3D elastoplastic constitutive model for soils based on the characteristic stress. Computers and Geotechnics, **109**: 229-247. doi:10.1016/j.compgeo.2019.02.001.

Lu, D., Ma, C., Du, X., Jin, L., and Gong, Q. 2017. Development of a new nonlinear unified strength theory for geomaterials based on the characteristic stress concept. International Journal of Geomechanics, **17**(2): 04016058. doi:10.1061/(asce)gm.1943-5622.0000729.

Ma, C., Lu, D., Du, X., and Zhou, A. 2017. Developing a 3D elastoplastic constitutive model for soils: A new approach based on characteristic stress. Computers and Geotechnics, **86**: 129-140. doi:10.1016/j.compgeo.2017.01.003.

Mamou, A., Powrie, W., Clayton, C.R.I., and Priest, J.A. 2021. Suitability of empirical equations for estimating permanent settlement of railway foundation materials subjected to cyclic loading with principal stress rotation. Canadian Geotechnical Journal, **58**(10): 1603-1610. doi:10.1139/cgj-2020-0183.

Mauer, L. 1995. An interactive track-train dynamic model for calculation of track error growth. Vehicle System Dynamics, **24**(sup1): 209-221. doi:10.1080/00423119508969626.

McDonald, L.M., and Raymond, G.P. 1984. Repetitive load testing: reversal or rotation. Canadian Geotechnical Journal, **21**(3): 456-474. doi:10.1139/t84-050.

Mishra, D., Boler, H., Tutumluer, E., Hou, W., and Hyslip, J.P. 2017. Deformation and dynamic load amplification trends at railroad bridge approaches: Effects caused by high-speed passenger trains. Transportation Research Record, **2607**(1): 43-53. doi:10.3141/2607-07.

Momoya, Y., Sekine, E., and Tatsuoka, F. 2005. Deformation characteristics of railway roadbed and subgrade under moving-wheel load. Soils and Foundations, **45**(4): 99-118. doi:10.3208/sandf.45.4_99.

Nielsen, J.C.O., and Li, X. 2018. Railway track geometry degradation due to differential settlement of ballast/subgrade – Numerical prediction by an iterative procedure. Journal of Sound and Vibration, **412**: 441-456. doi:10.1016/j.jsv.2017.10.005.

Nimbalkar, S., and Indraratna, B. 2016. Improved performance of ballasted rail track using geosynthetics and rubber shockmat. Journal of Geotechnical and Geoenvironmental Engineering, **142**(8): 04016031. doi:10.1061/(asce)gt.1943-5606.0001491.

Nimbalkar, S., Punetha, P., and Kaewunruen, S. 2020. Performance improvement of ballasted railway tracks using geocells: present state of the art. *In* Geocells. Springer Transactions in Civil and Environmental Engineering. *Edited by* T.G. Sitharam and A. Hegde and S. Kolathayar. Springer, Singapore.

Odemark, N. 1949. Investigations as to the elastic properties of soils and design of pavements according to the theory of elasticity. Statens Vaginstitut, Meddelande **77**.

Paixão, A., Fortunato, E., and Calçada, R. 2014. Transition zones to railway bridges: Track measurements and numerical modelling. Engineering Structures, **80**: 435-443. doi:10.1016/j.engstruct.2014.09.024.

Paixão, A., Fortunato, E., and Calçada, R. 2015. A numerical study on the influence of backfill settlements in the train/track interaction at transition zones to railway bridges. Proceedings of the Institution of Mechanical Engineers, Part F: Journal of Rail and Rapid Transit, **230**(3): 866-878. doi:10.1177/0954409715573289.

Petalas, A.L., Dafalias, Y.F., and Papadimitriou, A.G. 2018. SANISAND-FN: An evolving fabric-based sand model accounting for stress principal axes rotation. International Journal for Numerical and Analytical Methods in Geomechanics, **43**(1): 97-123. doi:10.1002/nag.2855.

Poulos, H.G., and Davis, E.H. 1974. Elastic solutions for soil and rock mechanics. John Wiley & Sons, New York.

Powrie, W., Yang, L.A., and Clayton, C.R.I. 2007. Stress changes in the ground below ballasted railway track during train passage. Proceedings of the Institution of Mechanical Engineers, Part F: Journal of Rail and Rapid Transit, **221**(2): 247-262. doi:10.1243/0954409jrrt95.

Punetha, P., Nimbalkar, S., and Khabbaz, H. 2020. Analytical evaluation of ballasted track substructure response under repeated train loads. International Journal of Geomechanics, **20**(7): 04020093. doi:10.1061/(ASCE)GM.1943-5622.0001729.

Punetha, P., Nimbalkar, S., and Khabbaz, H. 2021a. Simplified geotechnical rheological model for simulating viscoelasto-plastic response of ballasted railway substructure. International Journal for Numerical and Analytical Methods in Geomechanics, **45**(14): 2019-2047. doi:10.1002/nag.3254.

Punetha, P., Maharjan, K., and Nimbalkar, S. 2021b. Finite Element Modeling of the Dynamic Response of Critical Zones in a Ballasted Railway Track. Frontiers in Built Environment, **7**: 1-11. doi:10.3389/fbuil.2021.660292.

Sañudo, R., dell'Olio, L., Casado, J.A., Carrascal, I.A., and Diego, S. 2016. Track transitions in railways: A review. Construction and Building Materials, **112**: 140-157. doi:10.1016/j.conbuildmat.2016.02.084.

Sassa, S., and Sekiguchi, H. 2001. Analysis of wave-induced liquefaction of sand beds. Géotechnique, **51**(2): 115-126. doi:10.1680/geot.2001.51.2.115.

Selig, E.T., and Waters, J.M. 1994. Track geotechnology and substructure management. Thomas Telford, London.

Shan, Y., Zhou, S., Wang, B., and Ho, C.L. 2020. Differential settlement prediction of ballasted tracks in bridge–embankment transition zones. Journal of Geotechnical and Geoenvironmental Engineering, **146**(9): 04020075. doi:10.1061/(asce)gt.1943-5606.0002307.

Shih, J.Y., Grossoni, I., and Bezin, Y. 2019. Settlement analysis using a generic ballasted track simulation package. Transportation Geotechnics, **20**: 100249. doi:10.1016/j.trgeo.2019.100249.

Sim, W.W., Aghakouchak, A., and Jardine, R.J. 2013. Cyclic triaxial tests to aid offshore pile analysis and design. Proceedings of the Institution of Civil Engineers - Geotechnical Engineering, **166**(2): 111-121. doi:10.1680/geng.12.00056.

Simo, J.C., and Hughes, T.J.R. 1998. Computational inelasticity. Interdisciplinary Applied Mathematics. Springer, New York.

Suiker, A.S.J., and de Borst, R. 2003. A numerical model for the cyclic deterioration of railway tracks. International Journal for Numerical Methods in Engineering, **57**(4): 441-470. doi:10.1002/nme.683.

Suiker, A.S.J., Selig, E.T., and Frenkel, R. 2005. Static and cyclic triaxial testing of ballast and subballast. Journal of Geotechnical and Geoenvironmental Engineering, **131**(6): 771-782. doi:10.1061/(ASCE)1090-0241(2005)131:6(771).

Symes, M.J., Gens, A., and Hight, D.W. 1988. Drained principal stress rotation in saturated sand. Géotechnique, **38**(1): 59-81. doi:10.1680/geot.1988.38.1.59.

Varandas, J.N., Hölscher, P., and Silva, M.A.G. 2013. Settlement of ballasted track under traffic loading: Application to transition zones. Proceedings of the Institution of Mechanical Engineers, Part F: Journal of Rail and Rapid Transit, **228**(3): 242-259. doi:10.1177/0954409712471610.

Varandas, J.N., Paixão, A., Fortunato, E., Zuada Coelho, B., and Hölscher, P. 2020. Long-term deformation of railway tracks considering train-track interaction and non-linear resilient behaviour of aggregates – a 3D FEM implementation. Computers and Geotechnics, **126**: 103712. doi:10.1016/j.compgeo.2020.103712.

Wang, H., and Markine, V. 2018. Modelling of the long-term behaviour of transition zones: Prediction of track settlement. Engineering Structures, **156**: 294-304. doi:10.1016/j.engstruct.2017.11.038.

Wang, H., Markine, V., and Liu, X. 2018. Experimental analysis of railway track settlement in transition zones. Proceedings of the Institution of Mechanical Engineers, Part F: Journal of Rail and Rapid Transit, **232**(6): 1774-1789. doi:10.1177/0954409717748789.

Wang, Z., Yang, Y., Lu, N., Li, Y., and Yu, H.S. 2019. Effects of the principal stress rotation in numerical simulations of geotechnical laboratory cyclic tests. Computers and Geotechnics, **109**: 220-228. doi:10.1016/j.compgeo.2019.01.023.

Waterways Experiment Station. 1954. Investigations of pressures and deflections for flexible pavements: Report no. 4: Homogeneous sand test section. U.S. Waterways Experiment Station 3-323, Vicksburg, Mississippi.

Wijewickreme, D., and Vaid, Y.P. 2008. Experimental observations on the response of loose sand under simultaneous increase in stress ratio and rotation of principal stresses. Canadian Geotechnical Journal, **45**(5): 597-610. doi:10.1139/t08-001.

Wu, Z.X., Yin, Z.Y., Dano, C., and Hicher, P.Y. 2020. Cyclic volumetric strain accumulation for sand under drained simple shear condition. Applied Ocean Research, **101**: 102200. doi:10.1016/j.apor.2020.102200.

Yang, L. 2013. Experimental study of soil anisotropy using hollow cylinder testing. PhD thesis, University of Nottingham.

Yang, L.A., Powrie, W., and Priest, J.A. 2009. Dynamic stress analysis of a ballasted railway track bed during train passage. Journal of Geotechnical and Geoenvironmental Engineering, **135**(5): 680-689. doi:10.1061/(ASCE)GT.1943-5606.0000032.

Yang, Y., and Yu, H.S. 2013. A kinematic hardening soil model considering the principal stress rotation. International Journal for Numerical and Analytical Methods in Geomechanics, **37**(13): 2106-2134. doi:10.1002/nag.2138.

Zhai, W.M., Wang, K.Y., and Lin, J.H. 2004. Modelling and experiment of railway ballast vibrations. Journal of Sound and Vibration, **270**(4-5): 673-683. doi:10.1016/s0022-460x(03)00186-x.

Table captions

Table 1. Constitutive parameters for plastic slider element for subgrade.

Table 2. Input parameters for geotechnical rheological model used in parametric study.

Table 3. Input parameters for geotechnical rheological model used in validation.

Table 4. Input parameters for ballast in the stiffer side.

Table 1. Constitutive parameters for plastic slider element for subgrade.

Reference	λ	κ	φ_c (°)	ξ	M_p	A	a_h	$s_{1\alpha}$	$s_{2\alpha}$
Cai et al. (2015)	0.004	0.002	36[a]	0.1	1.46[a]	0.1	0.03	0.7	0.05
Wijewickreme and Vaid (2008)	0.009	0.002	30	0.1	1.24	0.1	–	0.31	0.05
Yang (2013)	0.025[b]	0.005[b]	27[c]	0.1	1.64	0.12	–	0.1	0.05
Wu et al. (2020)	0.03[d]	0.003	32.6[e]	0.27	1.31[e]	0.45	0.0175	0.7	0.05

Note: values taken from [a]Kong et al. (2019); [b]Altaee et al. (1992); [c]Wang et al. (2019); [d]Altuhafi et al. (2018); [e]Sim et al. (2013).

Table 2. Input parameters for geotechnical rheological model used in parametric study.

Layer	Variable	Unit	Value
Ballast	Young's modulus (E_b)	MPa	200[a]
	Poisson's ratio (v_b)	–	0.3[b,c]
	Shear stiffness (k_b^s)	MN/m	78.4[c,d]
	Density (ρ_b)	kg/m^3	1760[b,c]
	Thickness (h_b)	mm	300
	Reference void ratio on CSL (Γ)	–	1.4[*c]
	Slope of CSL (λ)	–	0.1[*c]
	Critical stress ratio (M_{tc})	–	1.25[*c]
	Volumetric coupling parameter (N_v)	–	0.2[*c]
	State-dilatancy parameter (χ_{tc})	–	3[*c]
	Cyclic hardening parameter (a_h)	–	0.143[*c]
	Plastic hardening parameter (H)	–	50-250ψ[*c]
	Plastic softening parameter (Z)	–	10[e]
Subballast	Young's modulus (E_s)	MPa	115[a,c]
	Poisson's ratio (v_s)	–	0.4[c]
	Shear stiffness (k_s^s)	MN/m	476[c]
	Density (ρ_s)	kg/m^3	1920[b,c]
	Thickness (h_s)	mm	150
	Reference void ratio on CSL (Γ)	–	0.9[*c]
	Slope of CSL (λ)	–	0.05[*c]
	Critical stress ratio (M_{tc})	–	1.15[*c]
	Volumetric coupling parameter (N_v)	–	0.3[*c]
	State-dilatancy parameter (χ_{tc})	–	4.2[*c]
	Cyclic hardening parameter (a_h)	–	0.185[*c]
	Plastic hardening parameter (H)	–	160-260ψ[*c]
	Plastic softening parameter (Z)	–	20[e]
Subgrade	Young's modulus (E_g)	MPa	41[b]
	Poisson's ratio (v_g)	–	0.35[b]
	Shear stiffness (k_g^s)	MN/m	1600[c]
	Density (ρ_g)	kg/m^3	1920[b]
	Thickness (h_g)	mm	5000
	Slope of CSL (λ)	–	0.004[†]
	Slope of swelling line (κ)	–	0.002[†]
	Critical state friction angle (φ_c)	°	36[†] – 40
	Characteristic stress parameter (ξ)	–	0.1[†]
	Spacing parameter (A)	–	0.1[†]
	Cyclic hardening parameter (a_h)	–	0.03[†]
	Parameter to account for PSR ($s_{1\alpha}$)	–	0.7[†]
	Parameter to account for PSR ($s_{2\alpha}$)	–	0.05[†]

Note: ψ = state parameter; values taken from [a]Li et al. (2018); [b]Li et al. (2016); [c]Punetha et al. (2021a); [d]Zhai et al. (2004); [e]calibrated against field data reported by Mishra et al. (2017); [*]calibrated against cyclic triaxial test data reported by Suiker et al. (2005); [†]calibrated against hollow cylinder torsional shear test data reported by Cai et al. (2015).

Table 3. Input parameters for geotechnical rheological model used in validation.

Layer	Variable	Unit	Mishra et al. (2017)	Paixão et al. (2014)	
				Section 2	Section 4
Ballast (Layer 1)	Young's modulus (E_b)	MPa	184	130	130
	Poisson's ratio (v_b)	–	0.3	0.2	0.2
	Shear stiffness (k_b^s)	MN/m	2^b	78.4^a	78.4^a
	Density (ρ_b)	kg/m^3	1990	1530	1530
	Thickness (h_b)	mm	305	300	300
	Reference void ratio on CSL (Γ)	–	1.4^a	–	–
	Slope of CSL (λ)	–	0.1^a	–	–
	Critical stress ratio (M_{tc})	–	1.25^a	–	–
	Volumetric coupling parameter (N_v)	–	0.2^a	–	–
	State-dilatancy parameter (χ_{tc})	–	3^a	–	–
	Cyclic hardening parameter (a_h)	–	0.295^b	–	–
	Plastic hardening parameter (H)	–	$50\text{-}250\psi^a$	–	–
	Plastic softening parameter (Z)	–	10^b	–	–
Subballast (Layer 2)	Young's modulus (E_s)	MPa	19	200	200
	Poisson's ratio (v_s)	–	0.4	0.3	0.3
	Shear stiffness (k_s^s)	MN/m	1^b	476^a	476^a
	Density (ρ_s)	kg/m^3	2092	1935	1935
	Thickness (h_s)	mm	127	300	300
	Reference void ratio on CSL (Γ)	–	0.9^a	–	–
	Slope of CSL (λ)	–	0.05^a	–	–
	Critical stress ratio (M_{tc})	–	1.15^a	–	–
	Volumetric coupling parameter (N_v)	–	0.3^a	–	–
	State-dilatancy parameter (χ_{tc})	–	4.2^a	–	–
	Cyclic hardening parameter (a_h)	–	0.2^b	–	–
	Plastic hardening parameter (H)	–	$160\text{-}260\psi^a$	–	–
	Plastic softening parameter (Z)	–	20^b	–	–
Subgrade	Young's modulus (E_g)	MPa	49	1073	10000
	Poisson's ratio (v_g)	–	0.4	0.3	0.3
	Shear stiffness (k_g^s)	MN/m	50^b	500^b	1600^a
	Density (ρ_g)	kg/m^3	2092	1935	2200
	Thickness (h_g)	mm	2082	9200	9200
	Slope of CSL (λ)	–	0.005^a	–	–
	Slope of swelling line (κ)	–	0.001^a	–	–
	Critical state friction angle (φ_c)	°	40^b	–	–
	Characteristic stress parameter (ξ)	–	0.1^a	–	–
	Spacing parameter (A)	–	0.31^a	–	–
	Cyclic hardening parameter (a_h)	–	0.0022^b	–	–
	Parameter to account for PSR ($s_{1\alpha}$)	–	0.7^b	–	–
	Parameter to account for PSR ($s_{2\alpha}$)	–	0.05^b	–	–

Note: ψ is the state parameter; ^{a} taken from Punetha et al. (2021a); ^{b}values selected upon the basis of engineering judgement.

Table 4. Input parameters for ballast in the stiffer side.

Variable	Unit	Value
Young's modulus (E_b^r)	MPa	200[a]
Poisson's ratio (ν_b^r)	–	0.3[b,c]
Shear stiffness ($k_\mathrm{b}^{s,r}$)	MN/m	78.4[c,d]
Density (ρ_b^r)	kg/m^3	1760[b,c]
Thickness (h_b^r)	mm	300
Reference void ratio on CSL ($\varGamma$)	–	1.4[*c]
Slope of CSL (λ)	–	0.1[*c]
Critical stress ratio (M_tc)	–	1.25[*c]
Volumetric coupling parameter (N_v)	–	0.2[*c]
State-dilatancy parameter (χ_tc)	–	3[*c]
Cyclic hardening parameter (a_h)	–	0.143[*c]
Plastic hardening parameter (H)	–	50-250ψ[*c]
Plastic softening parameter (Z)	–	10[e]

Note: ψ = state parameter; values taken from [a]Li et al. (2018); [b]Li et al. (2016); [c]Punetha et al. (2021a); [d]Zhai et al. (2004); [e]calibrated against field data reported by Mishra et al. (2017); [*]calibrated against cyclic triaxial test data reported by Suiker et al. (2005).

Figure captions

Fig. 1. Geotechnical rheological model for the ballasted railway track.

Fig. 2. Comparison of response predicted using the present model with the experimental data reported by Cai et al. (2015) for subgrade soil under repeated loading conditions: (a) cyclic stress waveforms corresponding to one load cycle; accumulation of vertical strain with number of load cycles for (b) various CVSR at CSSR = 0; different CSSR at (c) CVSR = 0.15 and σ_c = 150 kPa; (d) CVSR = 0.25 and σ_c = 150 kPa; (e) CVSR = 0.15 and σ_c = 125 kPa.

Fig. 3. Comparison of the response predicted using the present model with the experimental data reported by Wijewickreme and Vaid (2008): (a) variation of stress ratio with deviatoric strain; (b) variation of volumetric strain with deviatoric strain.

Fig. 4. Comparison of the response predicted using the present model with the experimental data reported by Yang (2013).

Fig. 5. Comparison of the response predicted using the present model with the experimental data reported by Wu et al. (2020).

Fig. 6. Stress variation experienced by the substructure layers below a sleeper due to a moving wheel load.

Fig. 7. (a) Stress-time history for a soil element located 1200 mm below the sleeper bottom during a train passage; (b) variation of PSR angle with depth; variation of deviatoric stress with PSR angle at (c) 100 mm; (d) 350 mm; (e) 1200 mm below sleeper bottom.

Fig. 8. Effect of principal stress rotation on cumulative settlement: variation of settlement with (a) cumulative tonnage; variation with depth at a cumulative tonnage of (b) 1 MGT; (c) 5 MGT; (d) 20 MGT.

Fig. 9. Influence of axle load on cumulative settlement with and without the inclusion of PSR.

Fig. 10. Influence of granular layer thickness on cumulative settlement with and without the inclusion of PSR: (a) for variation in ballast thickness; (b) for variation in subballast thickness.

Fig. 11. Effect of considering PSR on the selection of granular layer thickness.

Fig. 12. Geotechnical rheological model for an open track-bridge transition.

Fig. 13. Comparison of predicted vertical track displacement with the field data reported by Paixão et al. (2014) at 0.9 m and 14.7 m from the bridge.

Fig. 14. Comparison of cumulative settlement predicted using the present method with the field data reported by Mishra et al. (2017).

Fig. 15. Effect of axle load on the behavior of critical zone with and without inclusion of PSR.

Fig. 16. Effect of granular layer thickness on the behavior of critical zone with and without considering the PSR: (a) for variation in ballast thickness; (b) for variation in subballast thickness.

Fig. 17. (a) Variation of settlement along the track length when subgrade friction angle in the improved zone is increased from 36 – 40°; (b) accumulation of settlement with tonnage at different sections of the critical zone.

Fig. A1. Yield surface during loading and unloading.

Fig. B1. (a) Variation of critical stress ratio with principal stress rotation angle [plotted using the data from Symes et al. (1988)]; (b) stress-dilatancy relationship at different principal stress rotation angles [modified from Sassa and Sekiguchi (2001)].

Fig. C1. Yield surface in the characteristic stress space.

Fig. D1. Influence of constitutive parameters on the accumulation of vertical strain: (a) effect of $s_{1\alpha}$; (b) effect of $s_{2\alpha}$.

Fig. E1. Variation of normalized vertical stress with depth below sleeper for elastic and plastic cases.

APPENDIX A

In the present approach, it is assumed that the size of the yield surface shrinks isotropically during unloading. This approach of reducing the yield surface size during the unloading stage was originally proposed by Carter et al. (1982). Since the parameter $\bar{\bar{p}}$ controls the size of the yield surface, its value is reduced using the following expression:

$$\frac{d\bar{\bar{p}}}{\bar{\bar{p}}} = \theta^* \frac{dp_{\mathrm{l}}}{p_{\mathrm{l}}} \tag{A1}$$

where,

$$p_{\mathrm{l}} = pe^{\left(\frac{q}{\bar{\bar{M}}p} - 1\right)} \tag{A2}$$

If the value of θ^* is taken as unity, the yield surface will shrink in such a way that it would always pass the current stress state. Carter et al. (1982) suggested that the value of θ^* must be less than unity. This is achieved by reducing the size of the yield surface in such a manner that the ratio $\frac{\bar{\bar{p}}}{p}$ is constant during unloading and equal to the value attained at the end of the loading stage.

Fig. A1 shows the evolution of the yield surface during loading and unloading. Suppose the geomaterial is first loaded along the path A to B and then unloaded along the path B to E. During unloading, both the yield surface and loading surface (which passes through the current stress state) shrink. However, the yield surface shrinks less than that of the loading surface. Now, if the geomaterial is unloaded to point D, both yield and loading surfaces will shrink further. If the geomaterial is reloaded from point C to point B through point E, it will show elastic behavior till point E is reached. Subsequently, the yield and loading surfaces will expand together until point B is reached, thereby generating plastic deformations.

APPENDIX B

Sassa and Sekiguchi (2001) extended the generalized plasticity model by rendering the loading function, plastic potential function, and the plastic modulus as a function of angle 'α'. In the extended generalized plasticity model, the stress-dilatancy equation was given by:

(B1) $$D^p = \{1 + a'(\alpha)\}\{M_g(\alpha) - q^*/p^*\}$$

where D^p is the dilatancy; q^* and p^* are the deviatoric and hydrostatic stress invariants, respectively; M_g is the critical stress ratio, which was expressed as:

(B2) $$M_g(\alpha) = M_{g0} - U(\alpha) \cdot a^* \cdot M_{g0}$$

where $U(\alpha)$ is calculated using eq. (11c); M_{g0} is the value of M_g at $\alpha = 0$; a^* is a coefficient related to M_g. Eq. (B2) represents the reduction in the critical stress ratio with an increase in α (see Fig. B1). In the present study, a similar equation has been used to simulate the variation of critical stress ratio with α [see eq. (11a)].

The term $a'(\alpha)$ in eq. (B2) is calculated as:

(B3) $$a'(\alpha) = a_0 + b_0 \cdot U(\alpha)$$

where a_0 and b_0 are the model parameters. This equation represents the variation of the slope of the stress-dilatancy plot with the angle α [see Fig. B1(b)]. In the present study, a similar equation has been used to simulate the variation of the slope of the stress-dilatancy plot with α [see eq. (11b)].

APPENDIX C

Fig. C1 shows the yield surface in the characteristic stress space. It can be seen that the yield surface is smooth and convex.

APPENDIX D

A parametric analysis is conducted to understand the influence of constitutive parameters $s_{1\alpha}$ and $s_{2\alpha}$ on the response of the geomaterials. The nominal values of the constitutive parameters used in this study are the same as that previously calibrated using the experimental data reported by Cai et al. (2015) (see Table 1). The input loading for this analysis is shown in Fig. 2(a). The values of σ_c, CVSR, and CSSR are taken as 150 kPa, 0.25, and 1/6, respectively. The values of parameters $s_{1\alpha}$ and $s_{2\alpha}$ are varied between 0 and 0.9. Only one parameter is changed at a time, while nominal values are provided to other parameters.

Fig. D1(a) shows the influence of parameter $s_{1\alpha}$ on the accumulation of vertical strain. It can be observed that the cumulative vertical strain increases with an increase in $s_{1\alpha}$. This observation is reasonable as the value of $\hat{M}_\alpha$ decreases with an increase in $s_{1\alpha}$ [see eq. (11a)]. This leads to an increment in the magnitude of vertical strain [see eq. (18)]. Fig. D1(b) shows the effect of parameter $s_{2\alpha}$ on the accumulation of vertical strain. It can be observed that the cumulative vertical strain decreases with an increase in $s_{2\alpha}$. This reduction is due to an increase in Z_α with increasing $s_{2\alpha}$ [see eq. (11b)]. This increment in Z_α leads to a reduction in the magnitude of vertical strain [see eq. (18)].

APPENDIX E

A 3D finite element (FE) model of the ballasted railway track is developed using ABAQUS to compare the stress distribution when the track substructure layers are simulated using elastic and elastoplastic constitutive models. Fig. E1 shows the FE model of the ballasted railway track whose geometry is based on a section along Amtrak's northeast corridor in the USA. The track consists of rails supported by sleepers that rest on the multiple geotechnical layers (ballast, subballast, and subgrade). Only one half is modeled due to symmetry along the centerline of the track. The bottom boundary of the model is assumed as fixed, whereas dashpots are provided at the vertical boundaries to prevent the reflection of stress waves. The train is modeled as a multi-body system comprising of four wheels, four axles, and two bogies. The wheel-rail contact is modeled using Hertzian nonlinear contact theory. All the track components are discretized using eight-noded brick elements of type C3D8R.

Fig. E1 shows the stress distribution with depth calculated for the two cases: elastic and plastic. In the elastic case, all the substructure layers are simulated using the linear-elastic constitutive model. For the plastic case, the ballast is simulated using the Drucker-Prager model with a non-associated flow rule while the subballast and subgrade layers are modeled using the Mohr-Coulomb constitutive model with a non-associated flow rule. It can be observed from the figure that the stress distribution predicted in both cases is almost similar (a difference of about 12%).

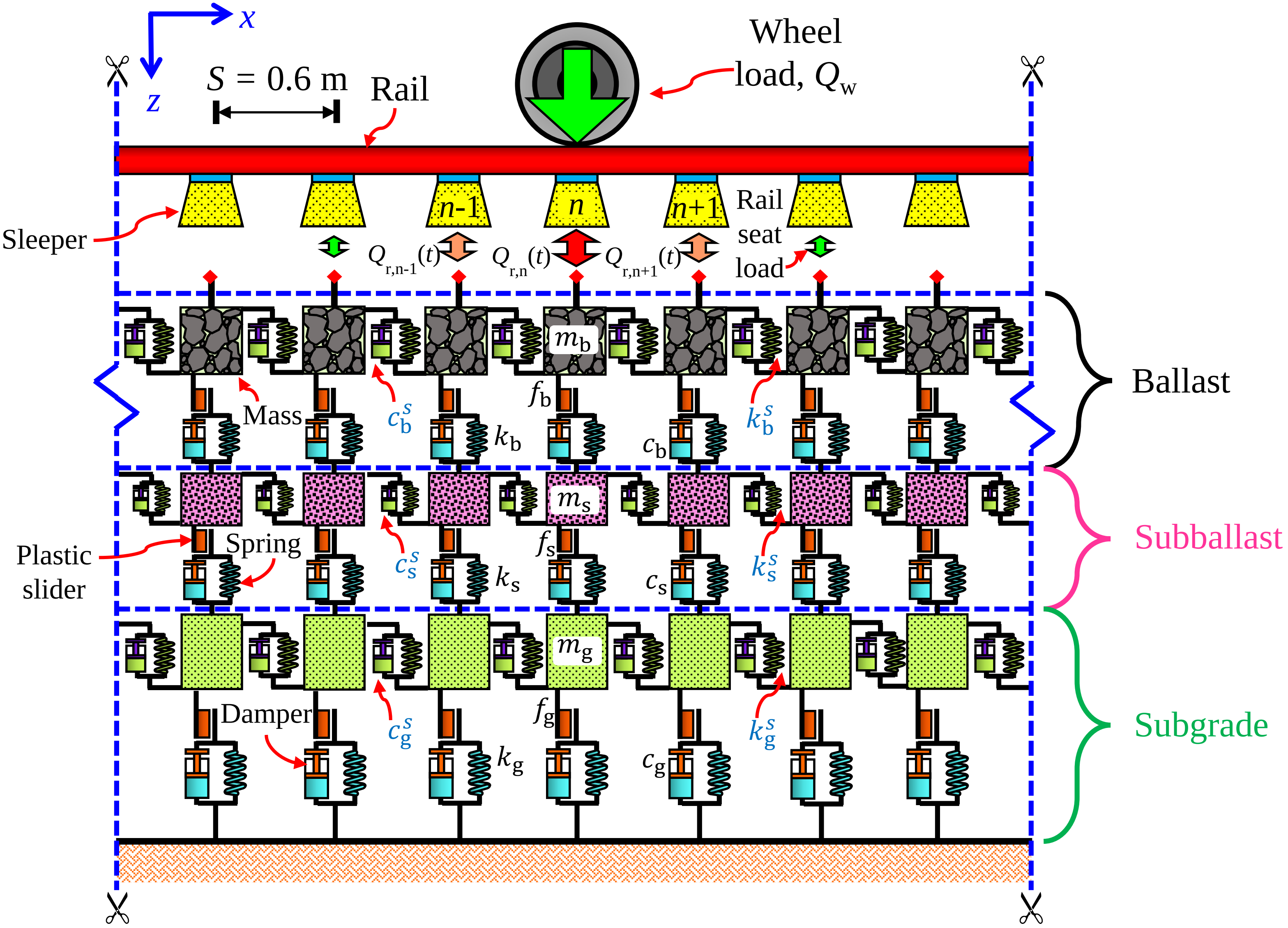

Fig. 1. Geotechnical rheological model for the ballasted railway track.

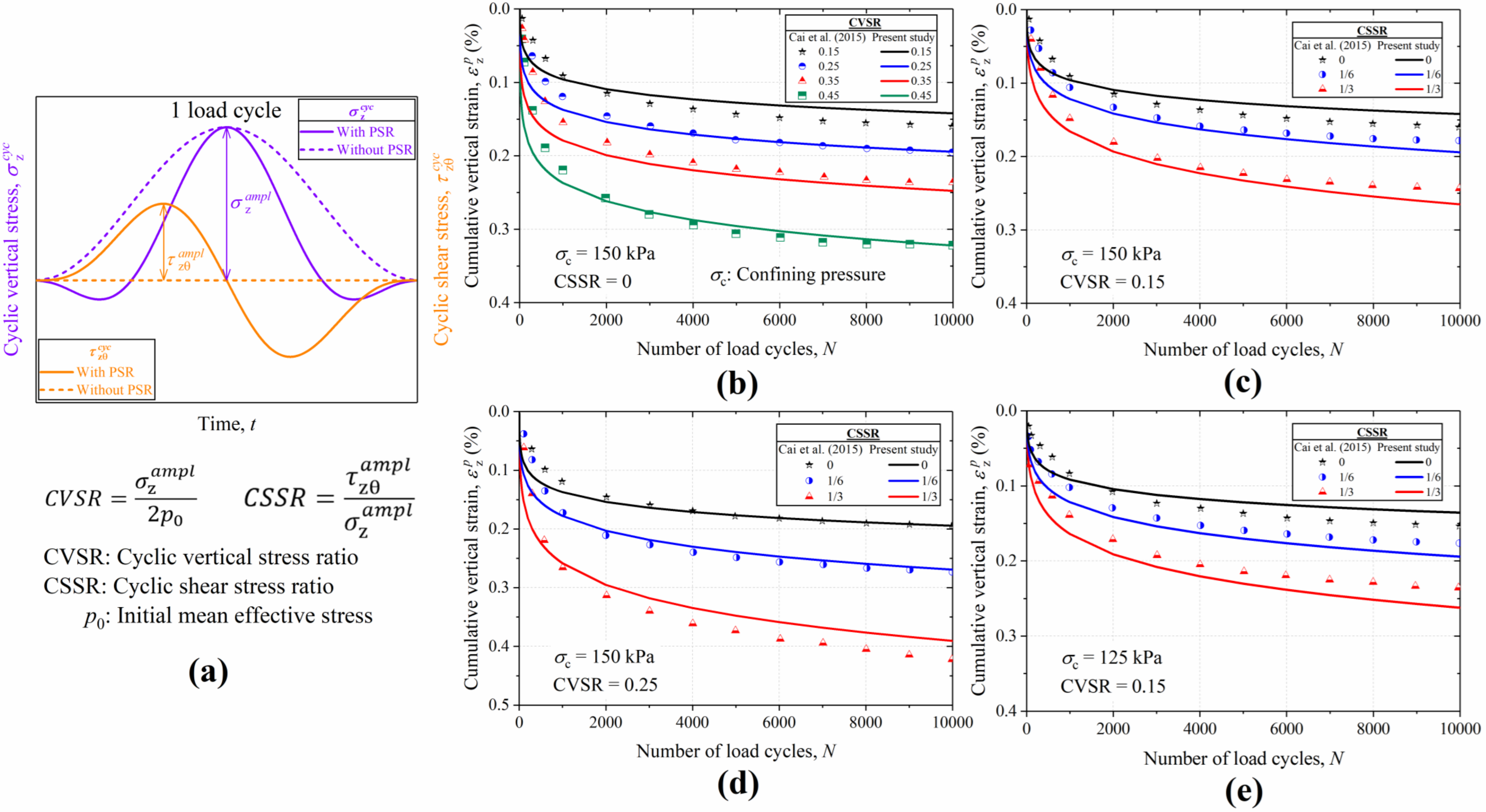

Fig. 2. Comparison of response predicted using the present model with the experimental data reported by Cai et al. (2015) for subgrade soil under repeated loading conditions: (a) cyclic stress waveforms corresponding to one load cycle; accumulation of vertical strain with number of load cycles for (b) various CVSR at CSSR = 0; different CSSR at (c) CVSR = 0.15 and σ_c = 150 kPa; (d) CVSR = 0.25 and σ_c = 150 kPa; (e) CVSR = 0.15 and σ_c = 125 kPa.

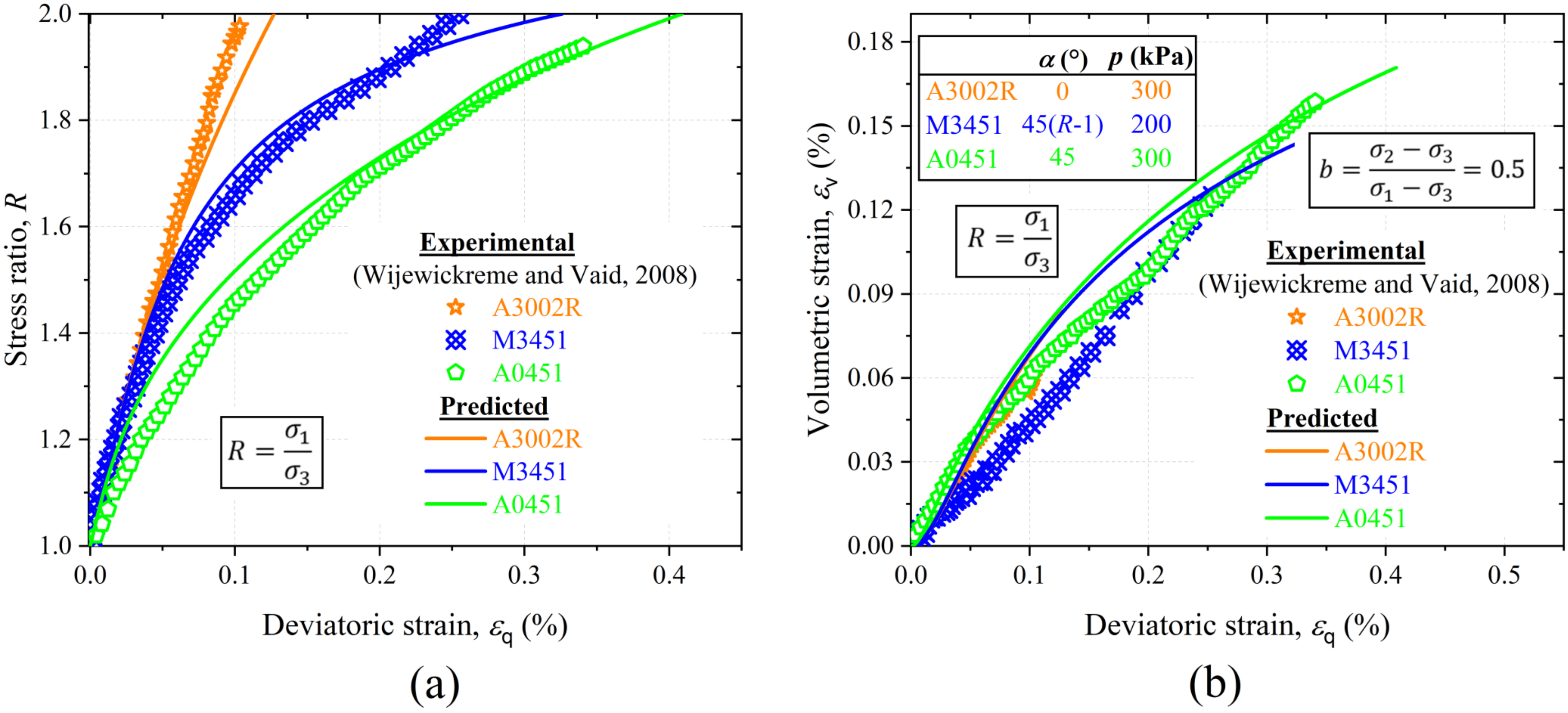

Fig. 3. Comparison of the response predicted using the present model with the experimental data reported by Wijewickreme and Vaid (2008): (a) variation of stress ratio with deviatoric strain; (b) variation of volumetric strain with deviatoric strain.

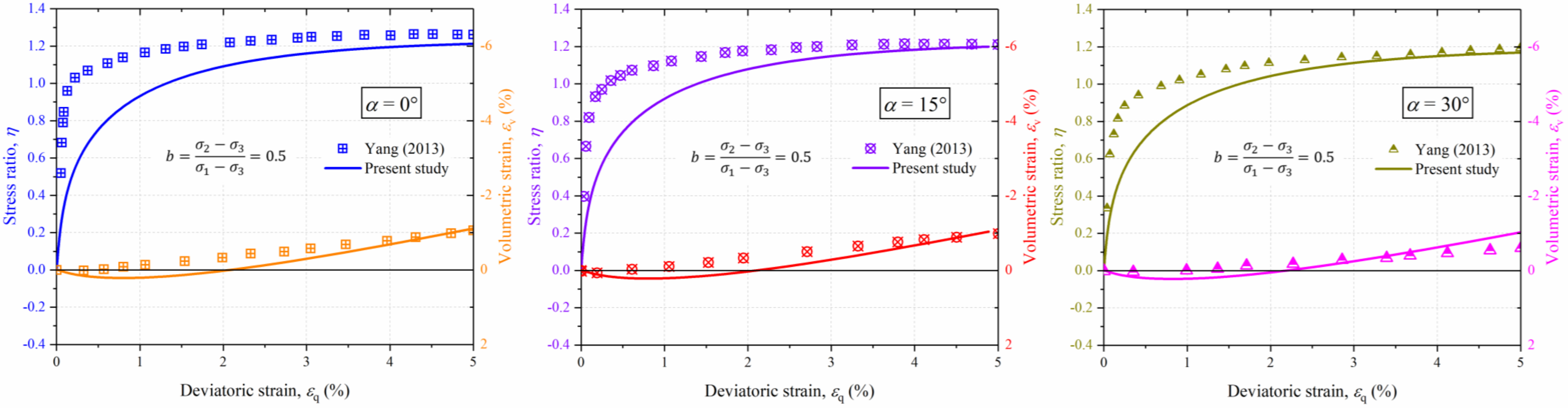

Fig. 4. Comparison of the response predicted using the present model with the experimental data reported by Yang (2013).

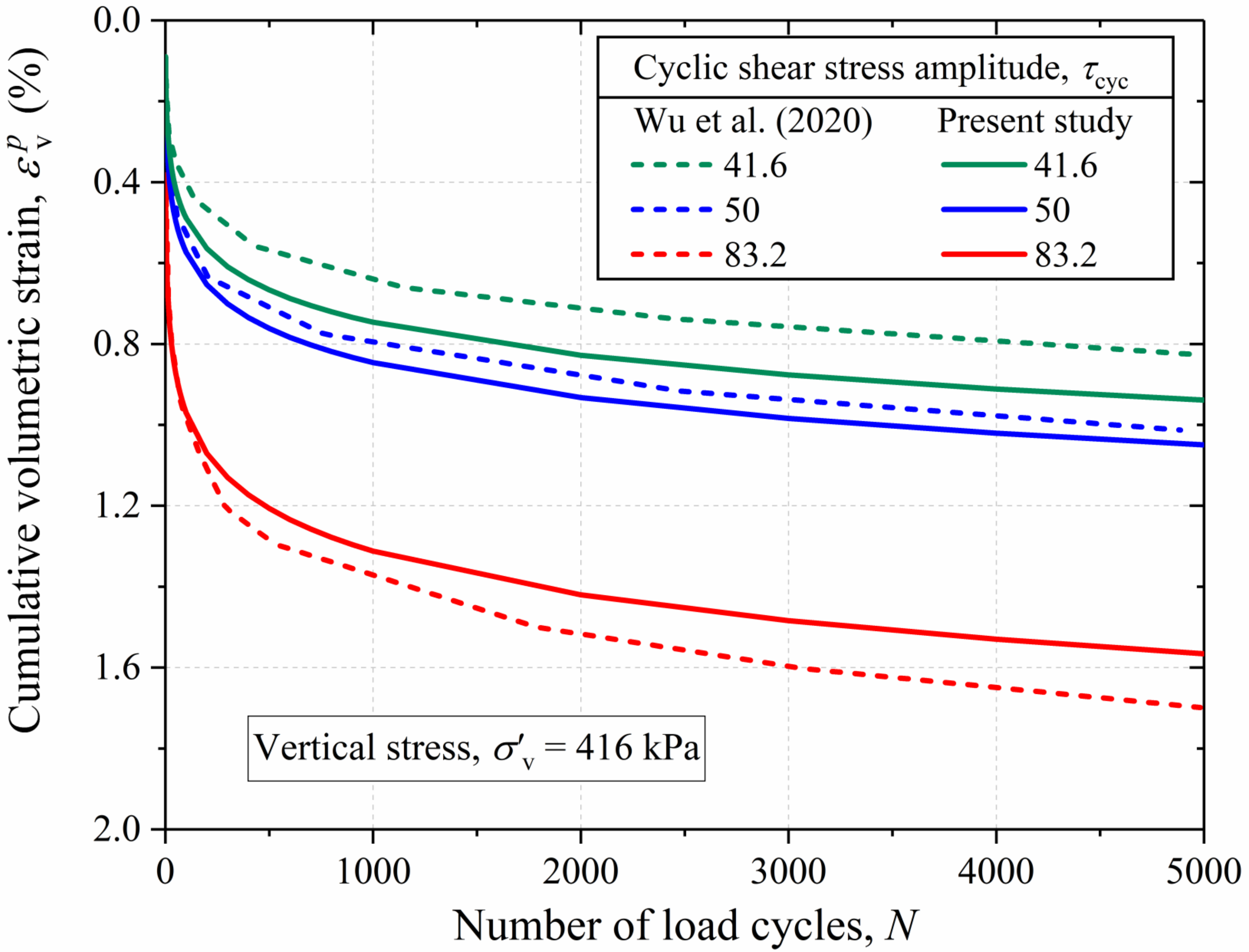

Fig. 5. Comparison of the response predicted using the present model with the experimental data reported by Wu et al. (2020).

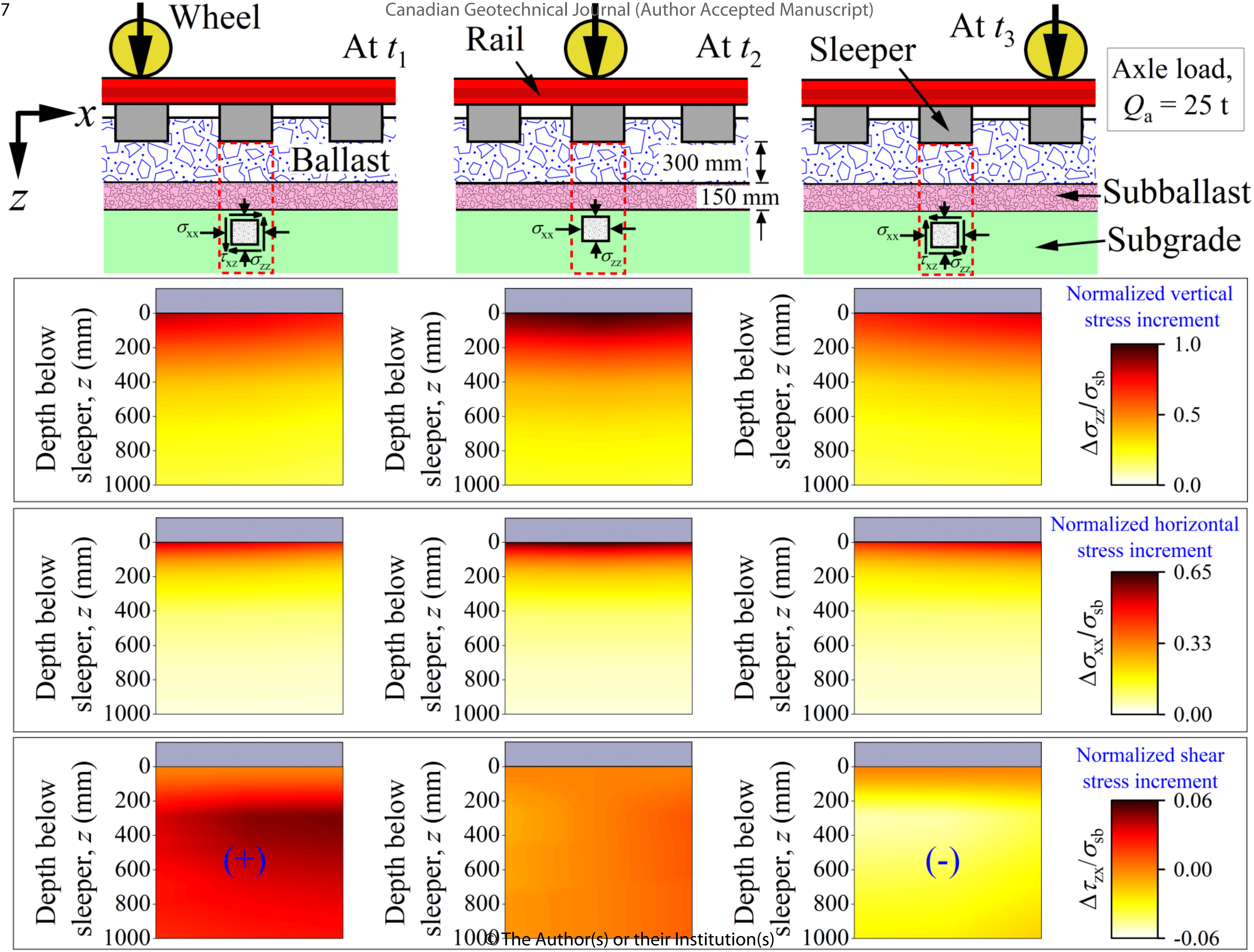

Fig. 6. Stress variation experienced by the substructure layers below a sleeper due to a moving wheel load.

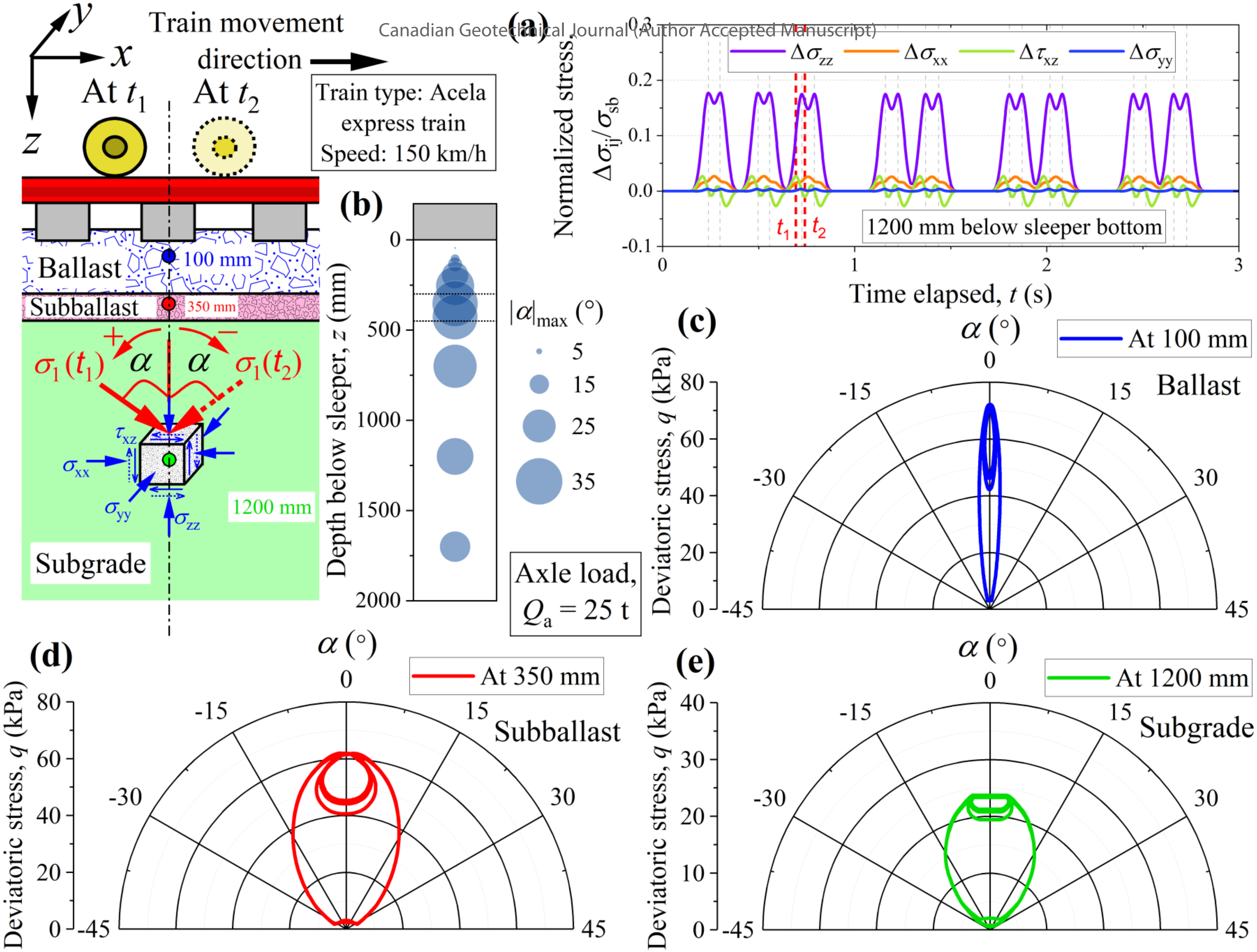

Fig. 7. (a) Stress-time history for a soil element located 1200 mm below the sleeper bottom during a train passage; (b) variation of PSR angle with depth; variation of deviatoric stress with PSR angle at (c) 100 mm; (d) 350 mm; (e) 1200 mm below sleeper bottom.

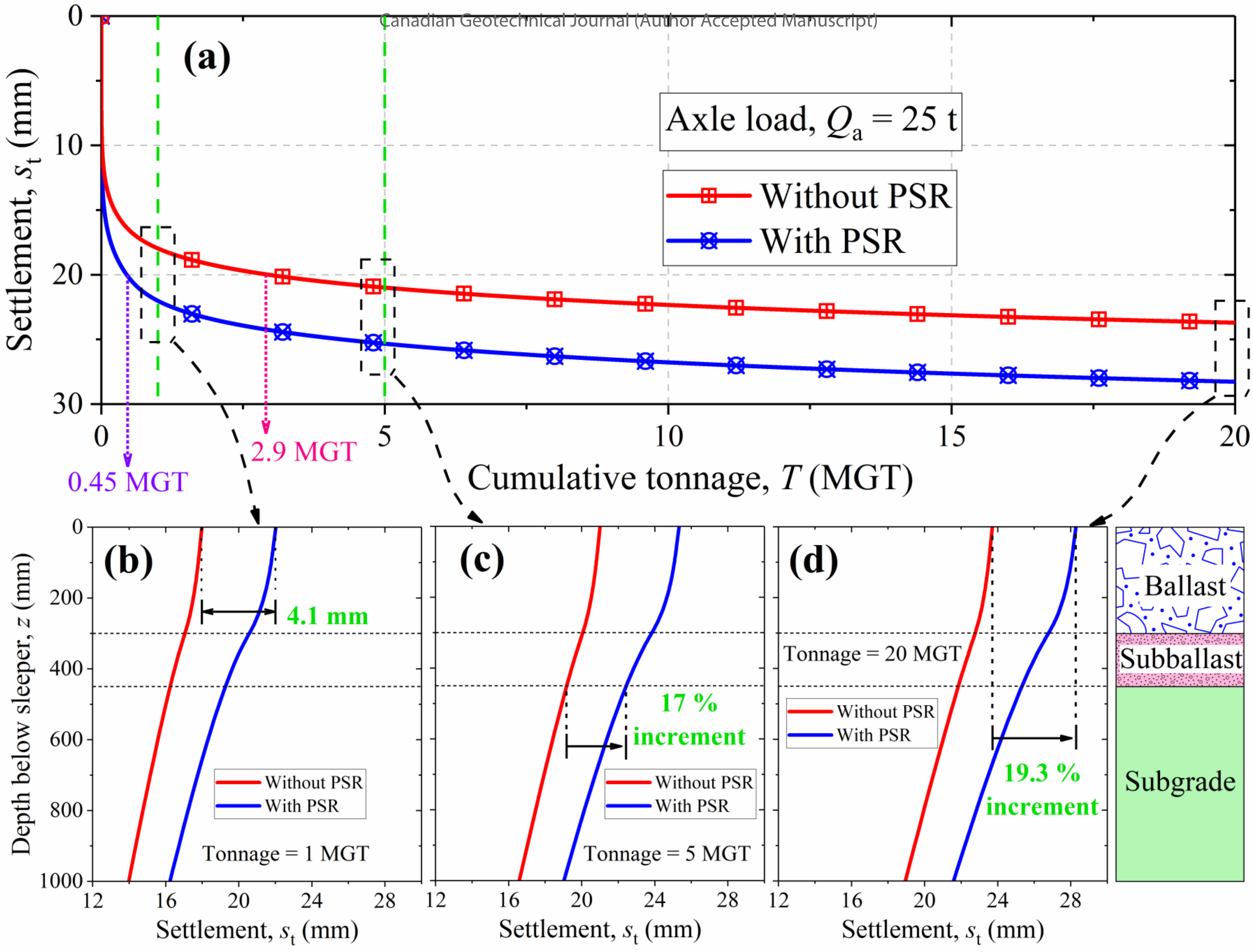

Fig. 8. Effect of principal stress rotation on cumulative settlement: variation of settlement with (a) cumulative tonnage; variation with depth at a cumulative tonnage of (b) 1 MGT; (c) 5 MGT; (d) 20 MGT.

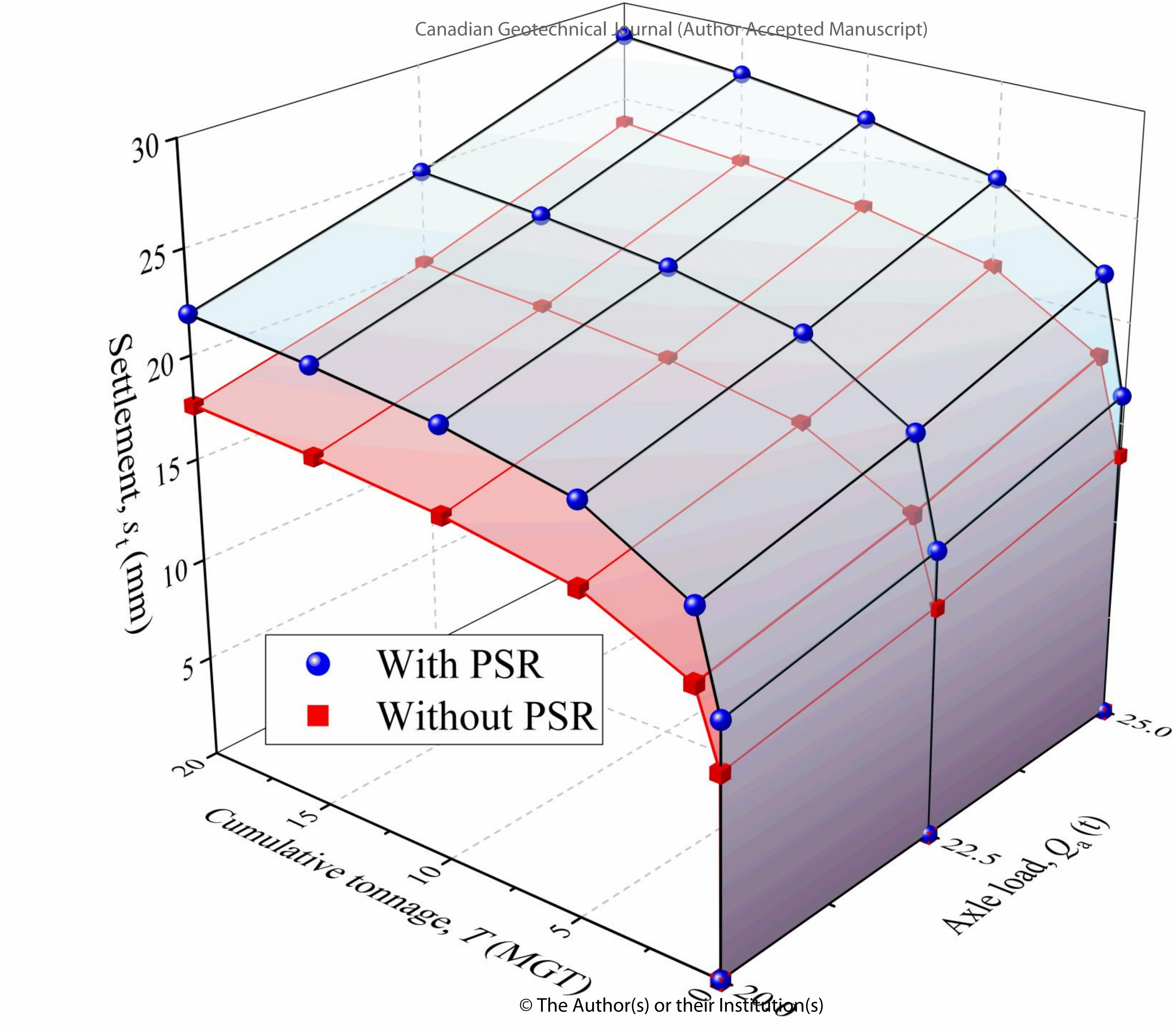

Fig. 9. Influence of axle load on cumulative settlement with and without the inclusion of PSR.

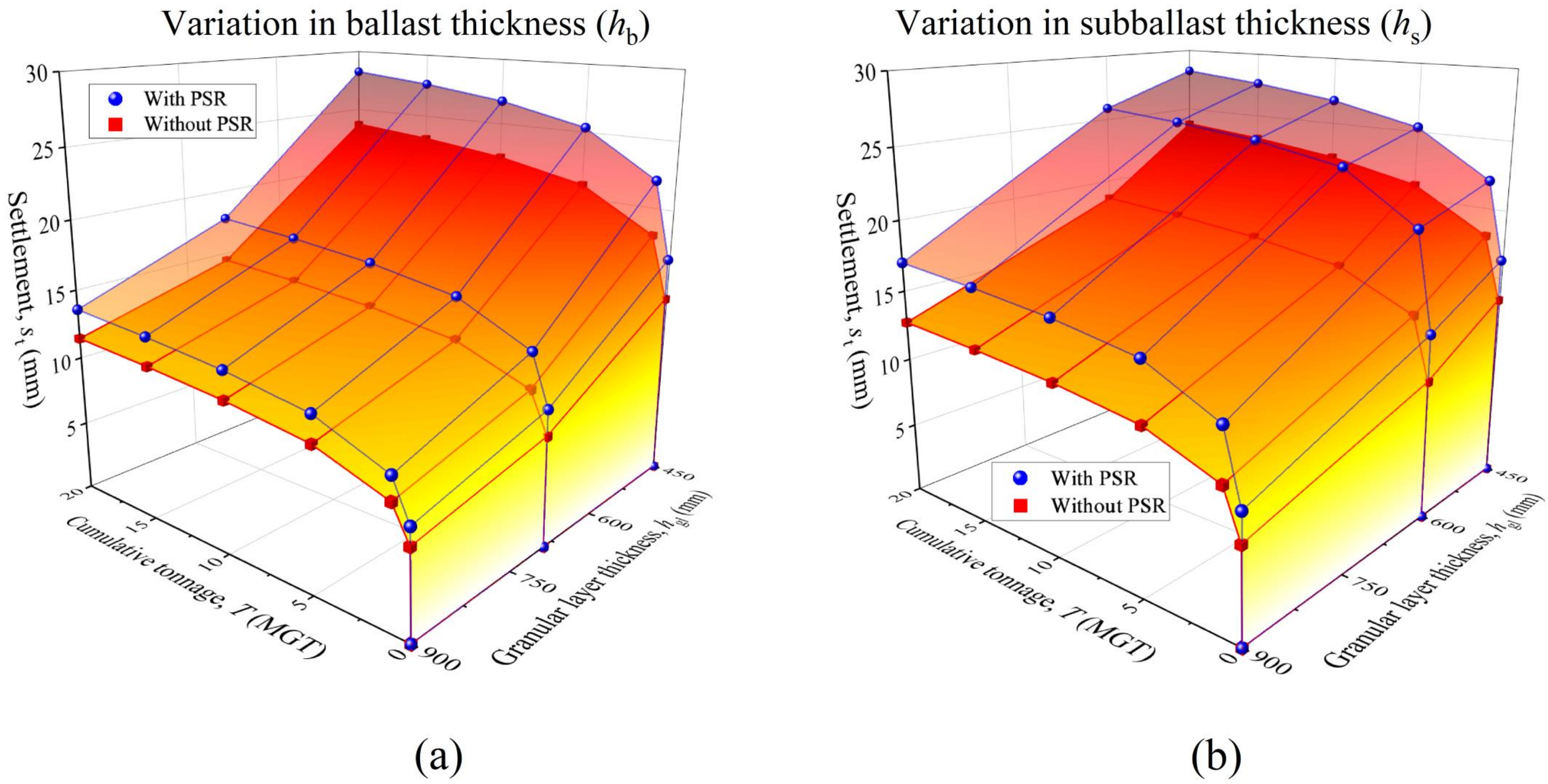

Fig. 10. Influence of granular layer thickness on cumulative settlement with and without the inclusion of PSR: (a) for variation in ballast thickness; (b) for variation in subballast thickness.

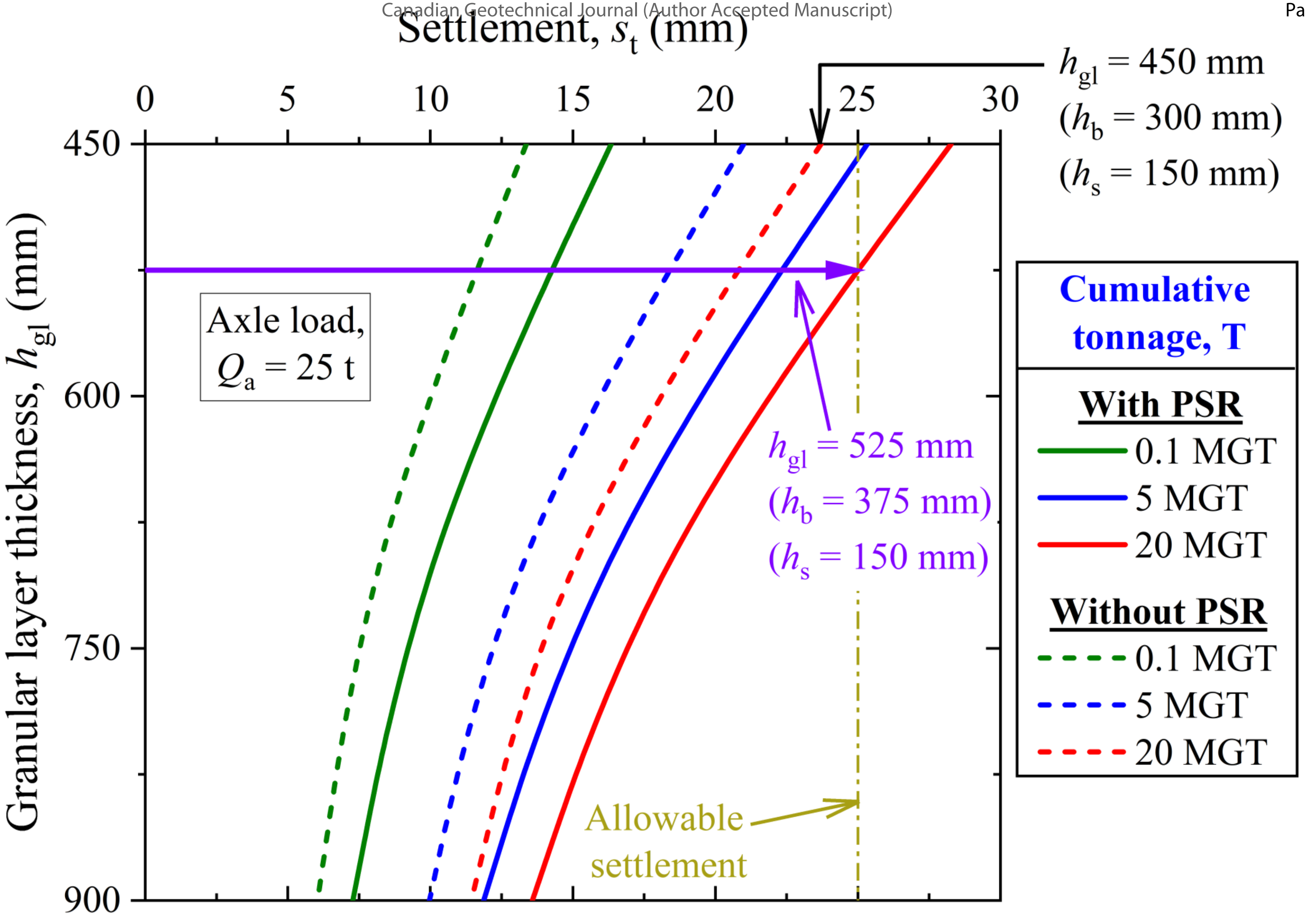

Fig. 11. Effect of considering PSR on the selection of granular layer thickness.

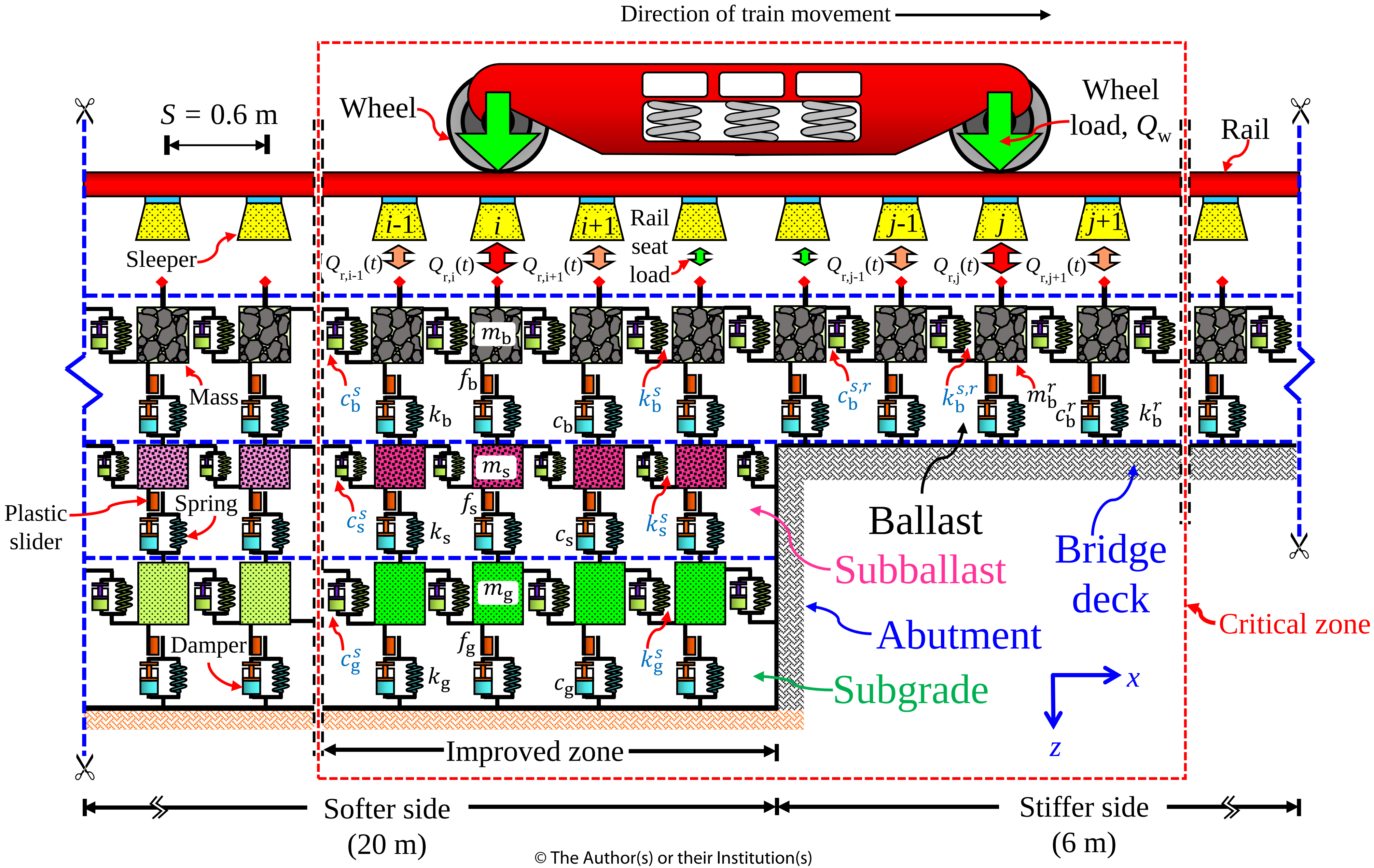

Fig. 12. Geotechnical rheological model for an open track-bridge transition.

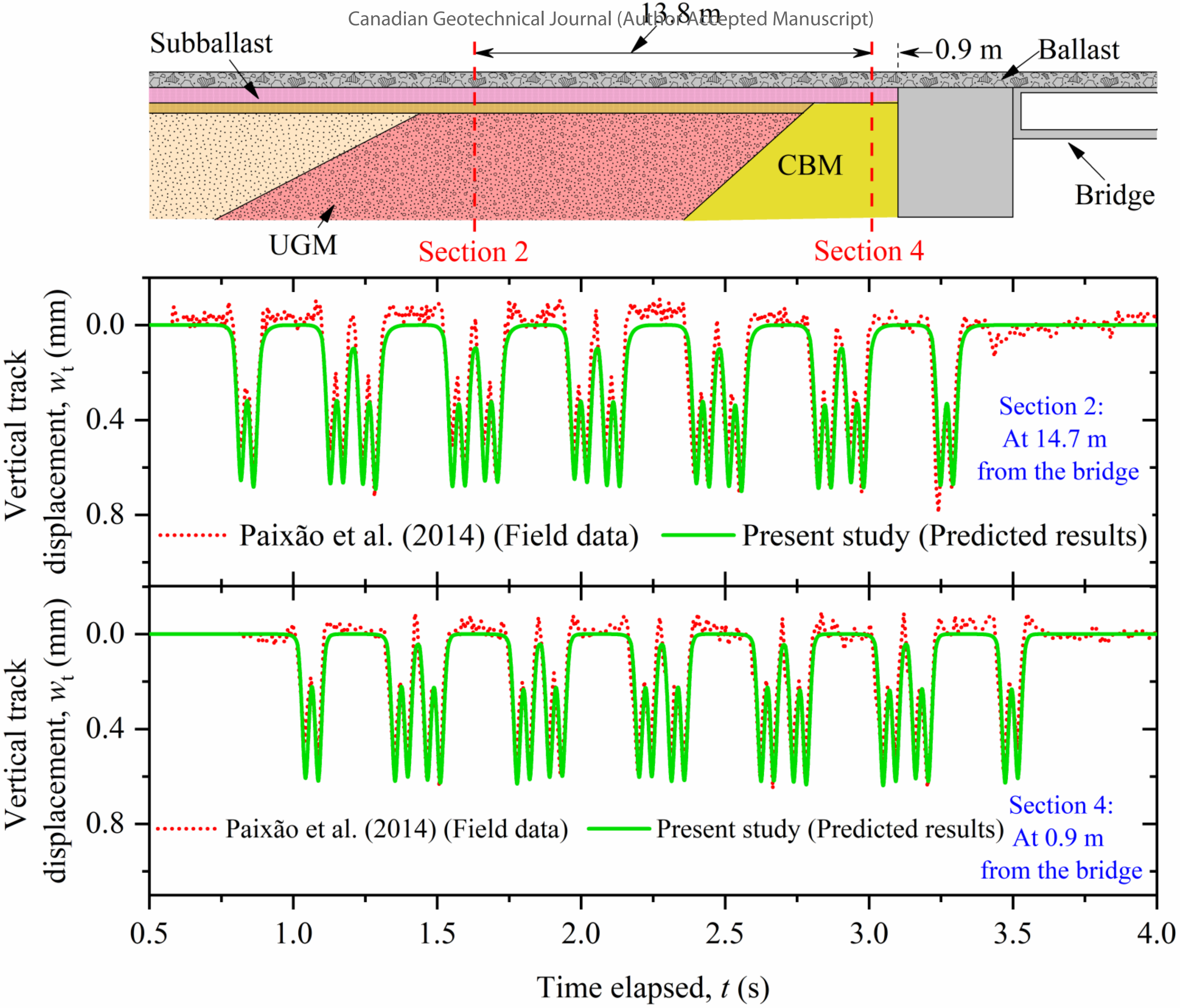

Fig. 13. Comparison of predicted vertical track displacement with the field data reported by Paixão et al. (2014) at 0.9 m and 14.7 m from the bridge.

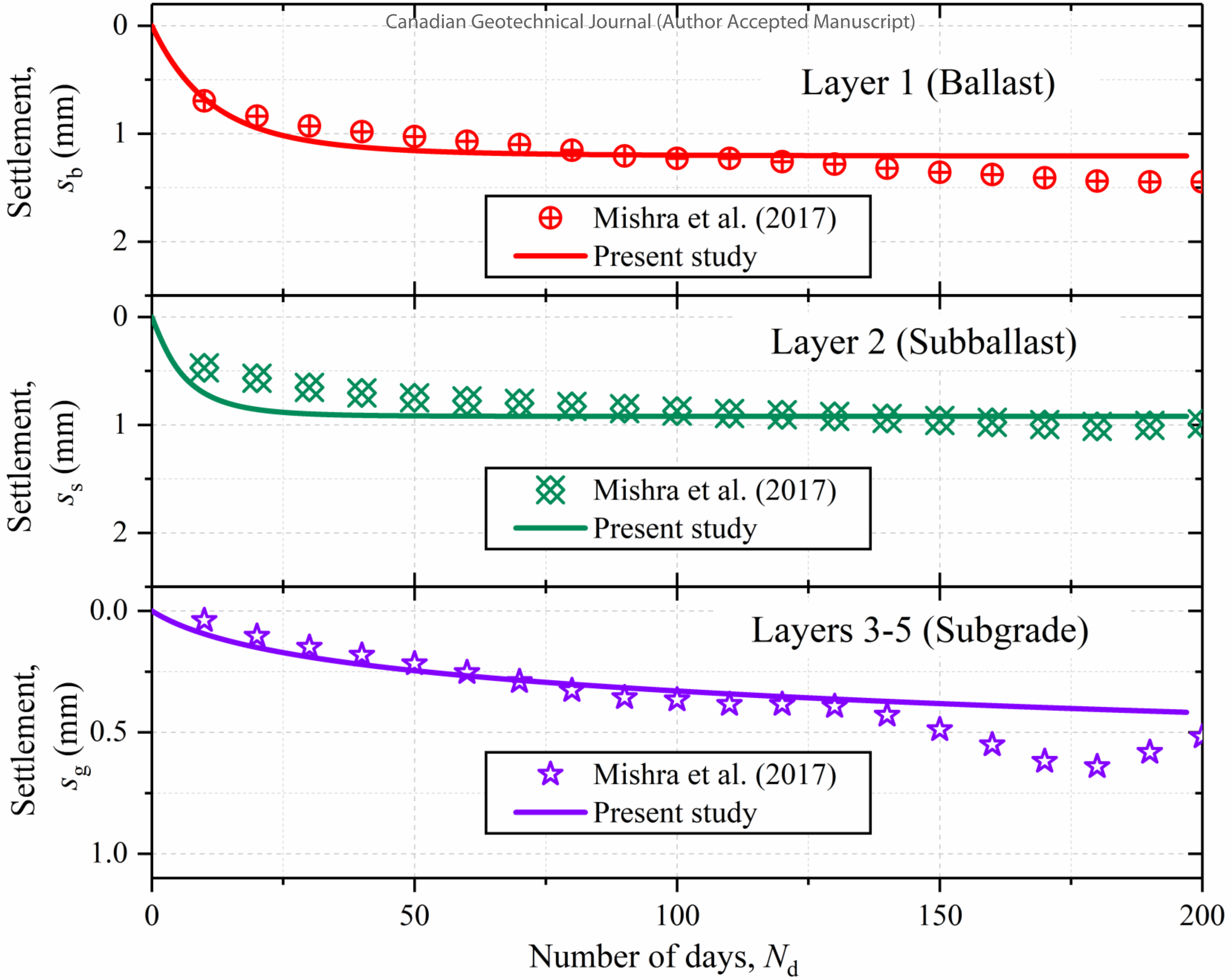

Fig. 14. Comparison of cumulative settlement predicted using the present method with the field data reported by Mishra et al. (2017).

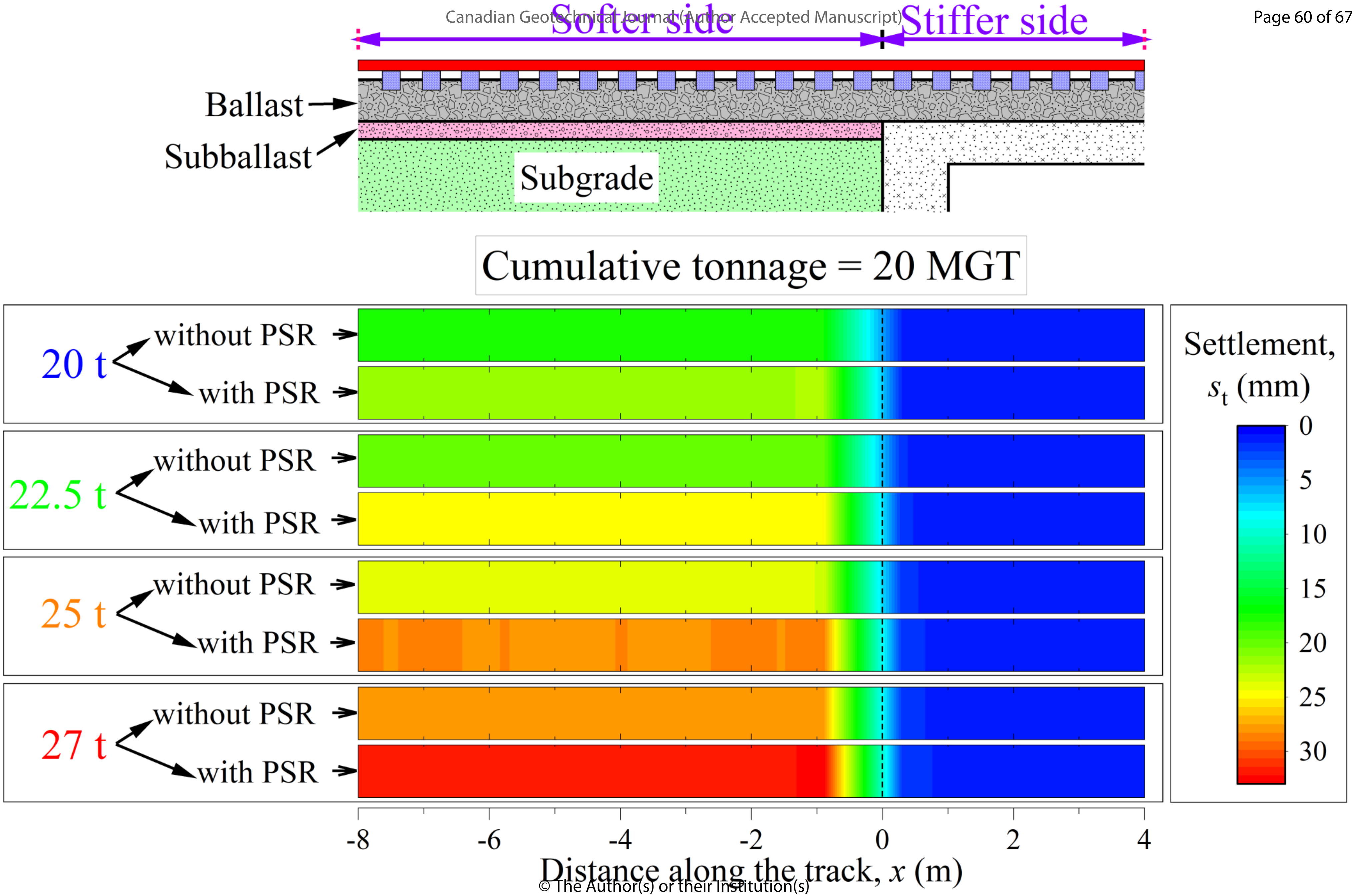

Fig. 15. Effect of axle load on the behavior of critical zone with and without inclusion of PSR.

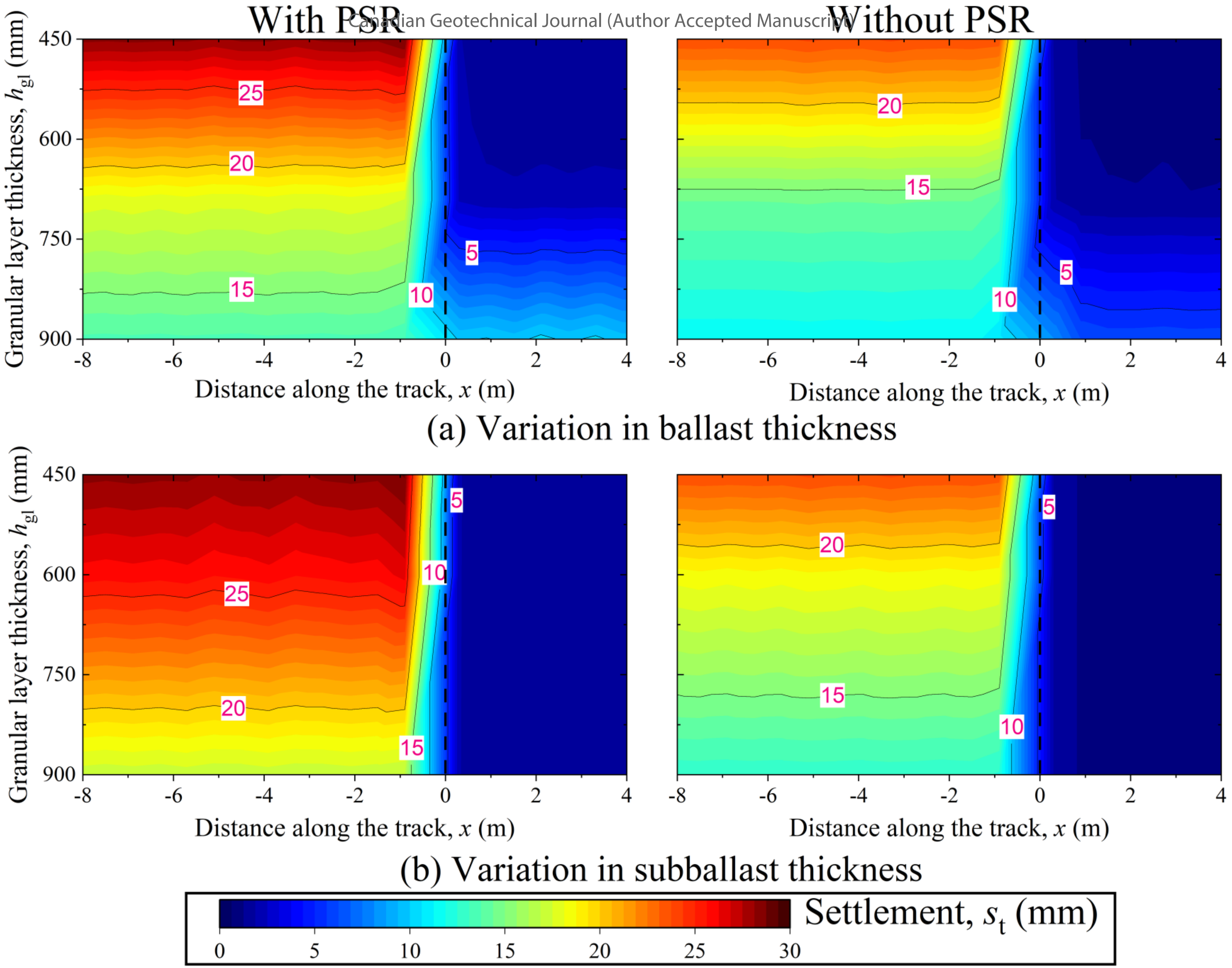

(a) Variation in ballast thickness

(b) Variation in subballast thickness

Fig. 16. Effect of granular layer thickness on the behavior of critical zone with and without considering the PSR: (a) for variation in ballast thickness; (b) for variation in subballast thickness.

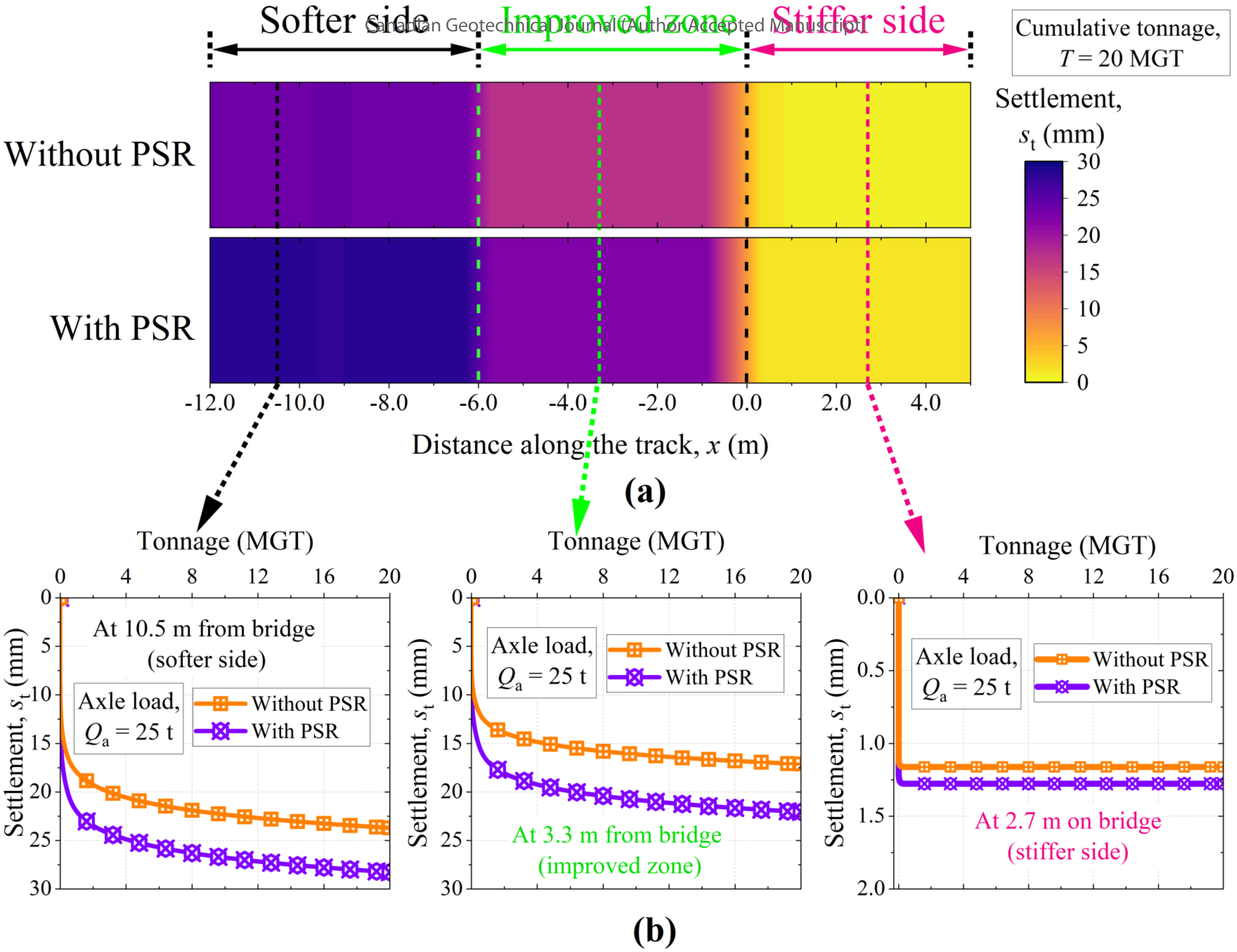

Fig. 17. (a) Variation of settlement along the track length when subgrade friction angle in the improved zone is increased from 36 – 40°; (b) accumulation of settlement with tonnage at different sections of the critical zone.

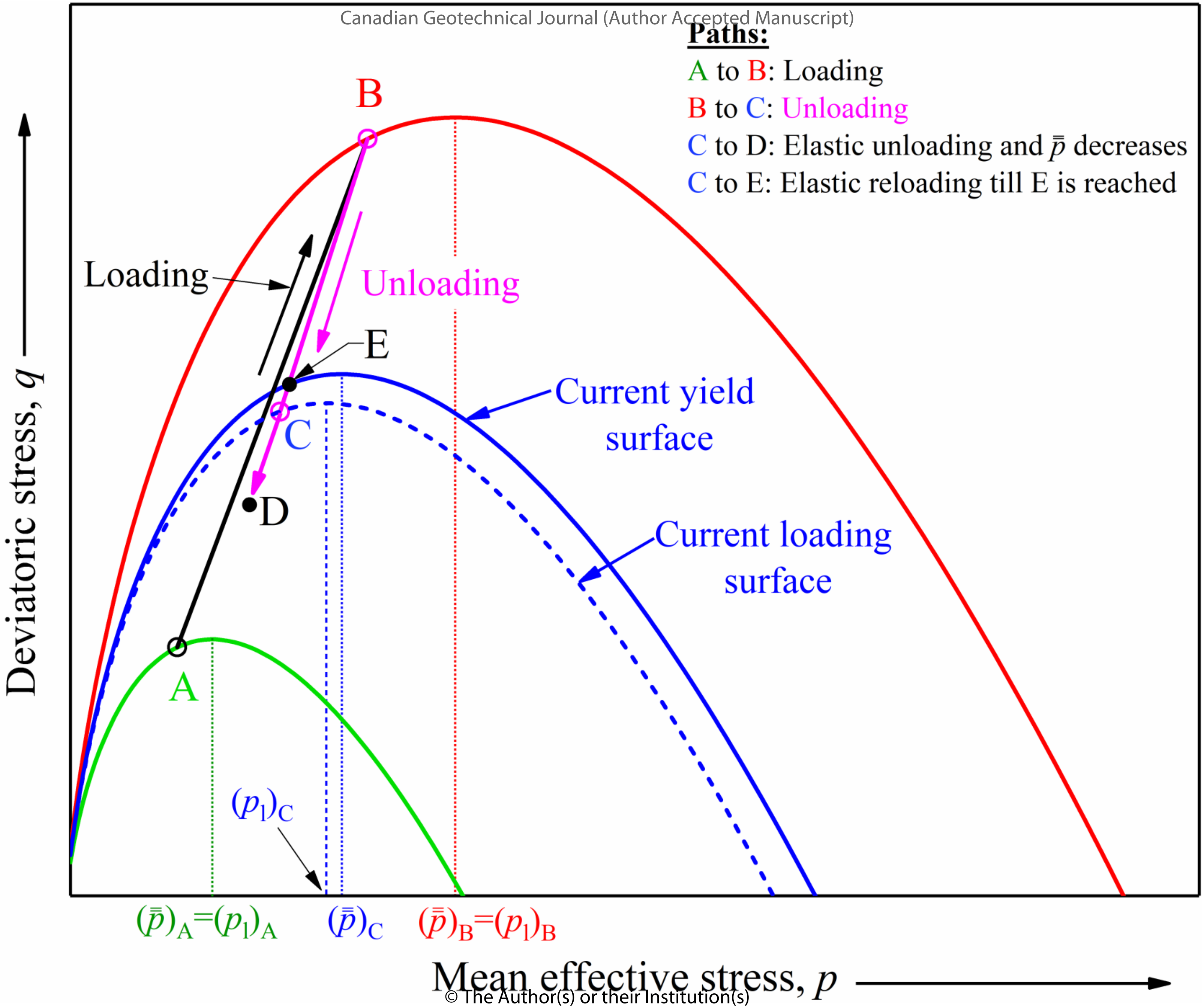

Fig. A1. Yield surface during loading and unloading.

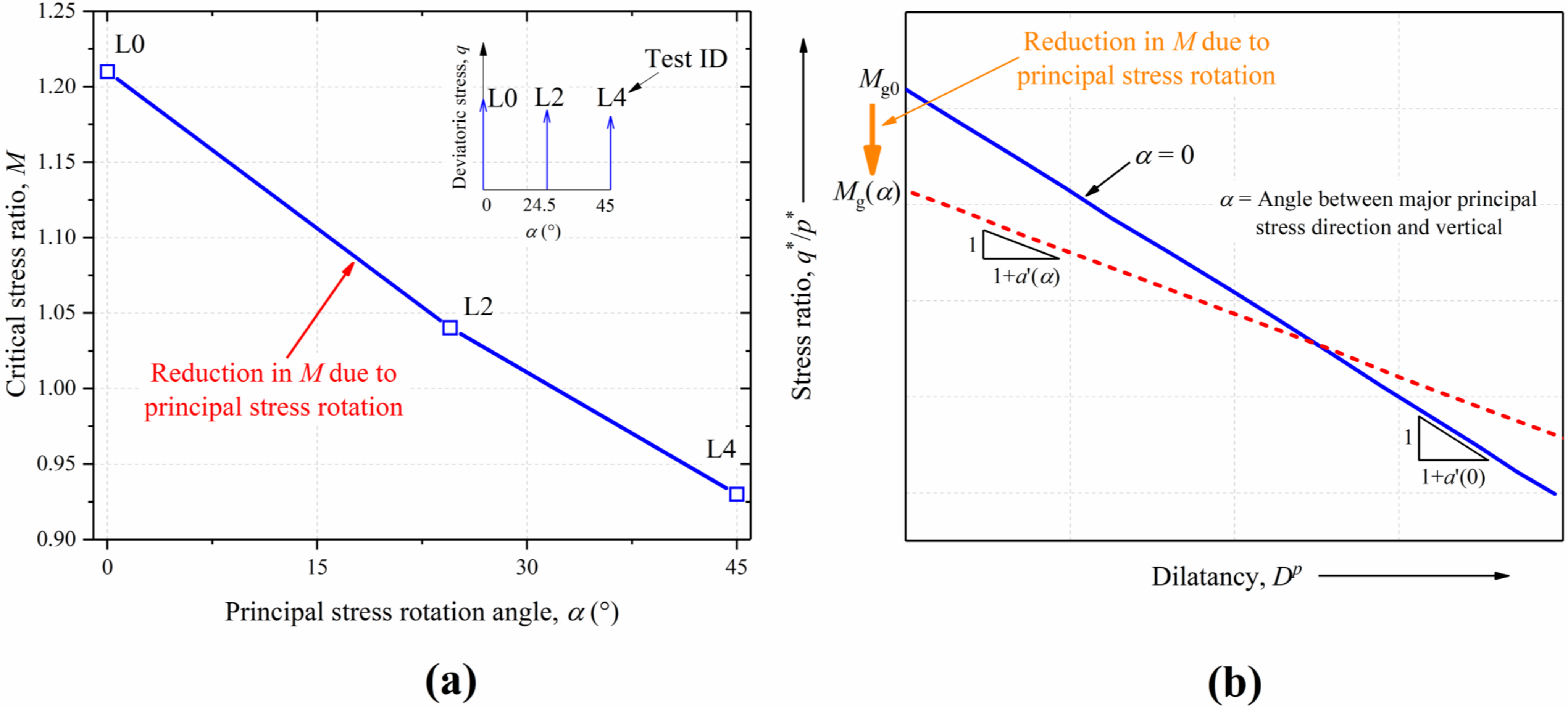

Fig. B1. (a) Variation of critical stress ratio with principal stress rotation angle [plotted using the data from Symes et al. (1988)]; (b) stress-dilatancy relationship at different principal stress rotation angles [modified from Sassa and Sekiguchi (2001)].

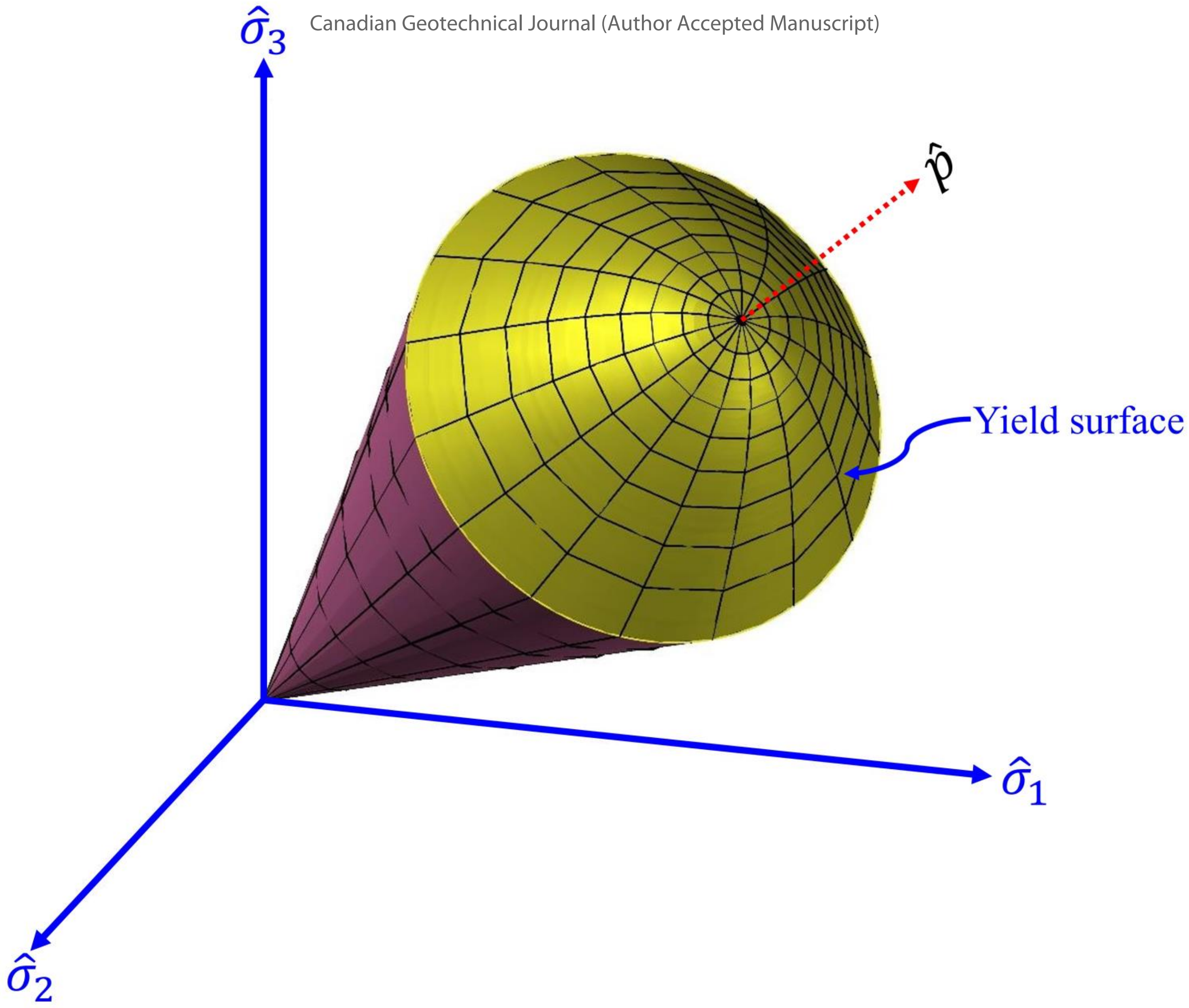

Fig. C1. Yield surface in the characteristic stress space.

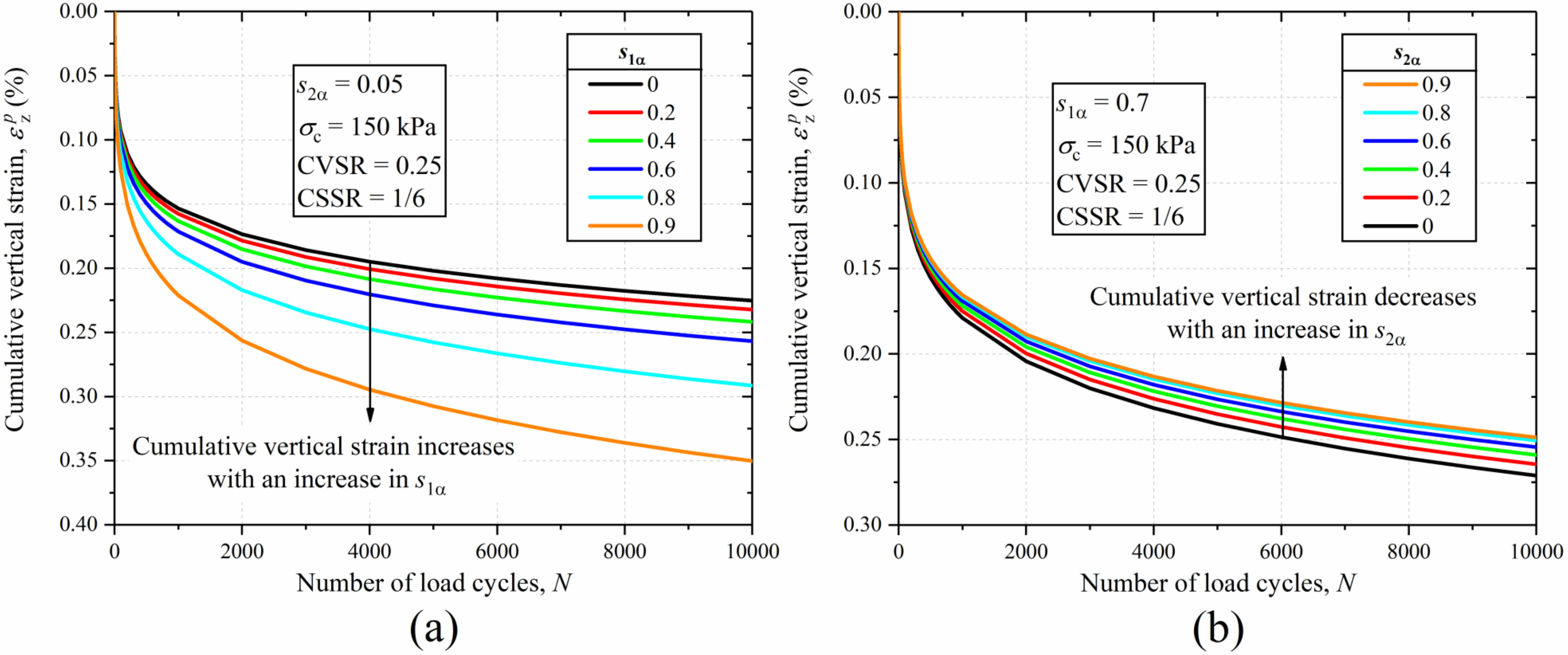

Fig. D1. Influence of constitutive parameters on the accumulation of vertical strain: (a) effect of $s_{1\alpha}$; (b) effect of $s_{2\alpha}$.

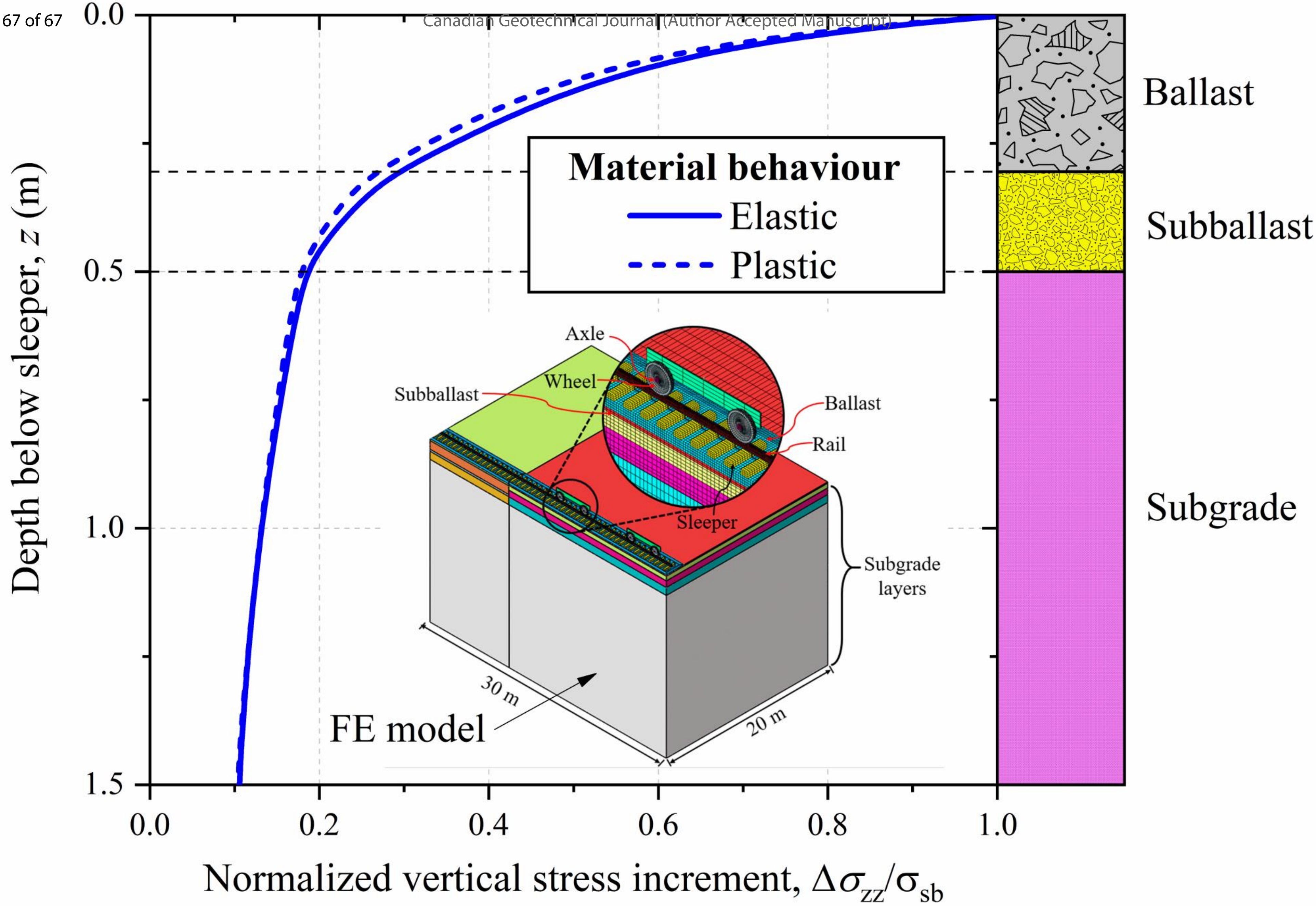

Fig. E1. Variation of normalized vertical stress with depth below sleeper for elastic and plastic cases.